Citation (APA)
Doosttalab, M., Ferreira, C. S., Ragni, D., Yu, W., & Rautmann, C. (2026). Evaluating dynamic stall models for thick wind turbine airfoils. *Renewable Energy*, *260*, Article 125096. https://doi.org/10.1016/j.renene.2025.125096

Renewable Energy 260 (2026) 125096

Contents lists available at ScienceDirect

Renewable Energy

journal homepage: www.elsevier.com/locate/renene

Evaluating dynamic stall models for thick wind turbine airfoils

Mehdi Doosttalab [a,b,*], Carlos Simão Ferreira [b], Daniele Ragni [b], Wei Yu [b], Christof Rautmann [a]

[a] Nordex Energy SE & Co. KG, Langenhorner Chaussee 600, Hamburg, 22419, Germany

[b] Faculty of Aerospace Engineering, Delft University of Technology, Kluyverweg 1, Delft, 2629 HS, Netherlands

ARTICLE INFO

Keywords:
Wind turbine
Flatback airfoil
Vortex generator
Dynamic stall models

ABSTRACT

The accuracy of the Beddoes–Leishman and Risø dynamic stall models is evaluated against experiments on thick wind turbine airfoils with a relative thickness of 35% and trailing edge thicknesses of 10% and 2%, both with and without vortex generators. The dynamic lift, drag, and pitching moment coefficients simulation results are compared with the measurements, obtained in the TU Delft LTT wind tunnel at a Reynolds number of $Re = 1 \times 10^6$ and dynamic reduced frequency of 0.064. The study revealed that while the aforementioned models successfully predicted the direction of the dynamic cycles, they inaccurately captured the dynamic stall behavior of thick flatback and non-flatback airfoils in all configurations, particularly in separated flows. There was no significant difference observed in the performance of the two models. The reasons for modeling failure are thoroughly examined from both fundamental and mathematical perspectives, and suggestions for improvements are provided. The findings raise concerns regarding the accuracy and reliability of the dynamic load assessment and aeroelasticity analysis for modern large wind turbines, using current dynamic stall models and underscore the necessity for enhancing the existing models.

1. Introduction

The wind energy sector has expanded rapidly in recent decades, driven by rising oil prices, growing energy demand, and environmental concerns. Wind turbines have scaled up significantly, with rotor diameters increasing from 10–15 m to 236 m (e.g. Vestas V236–15.0 MW model). This growth challenges engineers to balance lightweight and cost-effective materials with aerodynamic efficiency. Modern turbines use longer, more slender blades that endure greater static and dynamic loads than earlier design solutions. To enhance structural and aerodynamic performance while reducing weight, newer designs increase the thickness of the inboard-midspan blade section, particularly using flatback airfoils [1]. However, as the blade radius grows, elastic deformations also rise significantly [2], intensifying dynamic loads from wind gusts, pitch and yaw changes, wind shear, and aeroelastic torsion.

Leishman [3] classified unsteady aerodynamic loading into two types: periodic and aperiodic. Aperiodic sources include wind veer, atmospheric turbulence and wake induction. Periodic sources involve yaw misalignment, blade–tower interaction, and wind shear. These factors cause fluctuating angles of attack during blade rotation, leading to variations in loading, wake behavior, and inflow induction.

Dynamic flow conditions in wind turbines are typically described using reduced frequency ranges. Leishman [3] defined four regimes for rotorcraft: steady flow ($k = 0$), quasi-steady ($0 \leq k \leq 0.05$), unsteady ($k \geq 0.05$), and highly unsteady ($k \geq 0.2$). For wind energy, Pereira et al. [4] recommended accounting for unsteady effects when $k > 0.05$. Dynamic stall occurs when an airfoil undergoes a rapid change in angle of attack, disrupting the boundary layer and delaying flow reattachment beyond what is seen in static conditions. This causes stall to occur at higher angles than in the static polar and it delays the flow reattachment process. Dynamic stall can generate significant loads on wind turbines, potentially causing damage or reducing fatigue life.

Dynamic flow effects have been studied for decades [3]. Kramer [5] was among the first to identify three key mechanisms delaying stall onset. First, unsteady circulation during increasing angle of attack sheds into the wake, reducing lift. Second, virtual camber in a pitching airfoil lowers leading edge pressure and suction side gradients for a given lift coefficient [6]. Third, unsteady boundary layer behavior, particularly flow reversal caused by adverse pressure gradients, also plays a significant role in delaying stall onset [7]. Stall ultimately occurs due to a strong adverse pressure gradient near the leading edge, causing flow separation. Leishman [3] described how a free shear layer forms downstream, rolling into vortices that travel toward the trailing edge, enhancing pressure recovery and lift. This vortex shedding process has been widely studied [8]. While experiments have focused on dynamic stall onset [9], research on wind turbine airfoils remains limited. De Tavernier et al. [10] examined the effect of vortex generators on the dynamic stall of a vertical-axis wind turbine airfoil with a relative

* Corresponding author at: Nordex Energy SE & Co. KG, Langenhorner Chaussee 600, Hamburg, 22419, Germany.
E-mail address: Mdoosttalab@nordex-online.com (M. Doosttalab).

https://doi.org/10.1016/j.renene.2025.125096
Received 29 August 2025; Received in revised form 9 December 2025; Accepted 22 December 2025
Available online 2 January 2026

thickness of 25%. Choudhry et al. [11] studied the effect of vortex generators on an airfoil with a relative thickness of 21% to control dynamic stall in wind turbines.

Different stages of the dynamic stall phenomenon has been described by Leishman [3]. During the up-stroke (US) phase, the boundary layer flow reverses due to a reduced adverse pressure gradient caused by the pitch rate. In the second stage, leading edge separation forms a vortex that, if convected downstream along the suction side, can boost lift by 50–100% over the static maximum in low Mach number conditions. However, this also induces a sharp nose-down pitching moment. In stage four, during the down-stroke (DS) phase, the vortex exits at the trailing edge, and the flow becomes fully separated on the suction side, resembling the static flow field at the same angle of attack. Vortex shedding causes lift fluctuations. As the angle of attack decreases, reattachment begins but lags behind the static lift curve due to reverse camber effects from the negative pitch rate. Stage five marks fully reattached flow. The hysteresis across these stages reduces aerodynamic damping, potentially triggering aeroelastic issues on rotor blades [3].

Over the past decades, several dynamic stall models have been developed to simulate this complex phenomenon. These models aim to capture the transient lift, drag, and moment characteristics that arise during rapid changes in angle of attack, which are critical for accurate aeroelastic and load predictions in rotorcraft and wind turbine applications. Among the most widely recognized models are the Beddoes–Leishman (B-L) [12], Risø [13], Øye [14], ONERA [15], Boeing-Vertol [16], Goman-Khrabrov (G-K) [17], and Snel [18] dynamic stall models. Each of these formulations incorporates varying degrees of empirical and semi-empirical approaches, tailored to specific flow regimes and application domains. Among these, the B-L and Risø models are used extensively in the wind turbine aeroelastic and load assessments codes, i.e, OpenFAST [19], HAWC2 [20], and Bladed [21]. Each dynamic stall model includes two main categories of parameters: airfoil-dependent constants and flow-dependent time constants. The airfoil-dependent parameters are typically obtained from steady wind tunnel measurements, which provide reliable aerodynamic data under controlled conditions and serve as the basis for calibrating model constants. Because the experimental setup is relatively simple, such data are generally available for a wide range of airfoils. In contrast, flow-dependent parameters require unsteady wind tunnel measurements, which are significantly more complex, costly, and rarely conducted. Due to the limited availability of such data, the default time constants originally proposed in the respective model formulations are widely utilized by both the scientific and industrial communities [22], and are implemented in the aeroelastic simulation codes mentioned above. On the other hand, experimental validation of dynamic stall models for wind turbine-specific airfoils remains limited. Most available validations have been conducted on older airfoil designs originally developed for stall-regulated turbines. These airfoils typically feature maximum thicknesses of up to 24%, which may not accurately represent the aerodynamic behavior of modern, variable-speed pitch-regulated turbines [4].

Dynamic stall models, particularly the Beddoes–Leishman (B-L) model, have been extensively modified in the literature to improve prediction accuracy. For example, Huang et al. [23] employed CFD-based approaches to enhance the B-L model for the S809 and NACA0012 airfoils. Ge et al. [24] refined the B-L model for rough-surface airfoils and validated it using NREL S8XX wind turbine airfoils. Similarly, Liu et al. [25] improved the B-L model based on experimental dynamic measurements of the S809 airfoil. In addition to structural modifications, many studies have focused on adjusting model constants to account for airfoil geometry and flow conditions. Melani et al. [22] tuned the B-L model constants for the S809 airfoil. Faber [26] calibrated the Risø and Øye models using NACA00XX and NACA4415 airfoils. Adema et al. [27] adjusted the SNEL model for the NACA4415 and S809 airfoils, while Greenblatt et al. [28] optimized the G-K model for the NACA0018 airfoil. Finally, the procedure for determining ONERA model constants is thoroughly documented by McAlister et al. [29].

Airfoils with high relative thickness near the mid-span experience greater dynamic loads and fluctuations at high angles of attack. Due to their low stall angle of attack, active or passive flow control is essential. One effective approach involves using flatback airfoils [1] and/or vortex generators (VGs). Flatback airfoils are formed by thickening the aft camber line of sharp trailing edge profiles. Compared to conventional thick airfoils, they offer structural benefits and improved aerodynamics, including higher lift coefficients and steeper lift curves due to reduced adverse pressure gradients on the suction side [1]. VGs, in contrast, generate streamwise vortices that energize the boundary layer by mixing high-energy outer flow with low-momentum inner flow. This delays separation [30], increases lift, and raises the stall angle. VGs performance depends on their size, shape, and chordwise placement [31]. Moon et al. [32] assessed the impact of vortex generators on the power performance of a large wind turbine blade.

1.1. Objective of the current study

While thin airfoils have been extensively studied, the dynamic behavior of thick wind turbine airfoils remains comparatively underexplored. Accurate prediction of their dynamic behavior is essential for load assessment, aeroelasticity analysis, and turbine design, particularly for large modern wind turbines that incorporate a higher proportion of thick airfoils along the blade compared to older generation designs. However, the current understanding of how well existing dynamic stall models perform for thick conventional and flatback airfoils, especially when combined with VGs, especially from the maximum load stand point, is limited. The inaccuracies in predicting these properties can lead to significant errors in dynamic load predictions, compromising rotor blade design and turbine reliability. This study aims to address this gap by evaluating the accuracy of the B-L and Risø dynamic stall models for high relative thickness wind turbine airfoils for the first time, especially using the default time constants, which are being used by industry and scientific community. A wind tunnel campaign was conducted to measure the dynamic response of two thick airfoil types, conventional and flatback. The results of these measurements were used to examine the accuracy of the above models for various mean angles of attack within different lift curve regions, trailing edge gap, and VGs configurations in the free transition flow regime. The measurement matrix covers a broad range of configurations, providing a comprehensive dataset for evaluating dynamic stall models behavior in thick airfoils.

2. Methodology

2.1. Experimental setup

Experiments were conducted in the low-speed, low-turbulence wind tunnel (LTT) at Delft University of Technology [33], featuring a test section of $1250 \times 1250 \times 2600$ mm and a nozzle contraction ratio of $17.8 : 1$, yielding a turbulence intensity of 0.07% at 75 m/s. The tunnel reaches speeds up to 120 m/s and is powered by a 525 kW variable-speed electric motor. Aerodynamic tests were conducted on X-35-02 and X-FB-35-10 airfoils at a Reynolds number of $Re = 1.0 \times 10^6$. Both airfoils have 35% maximum thickness, 5% leading edge radius, and trailing edge thicknesses of 2% and 10%, respectively. X-FB-35-10 is the flatback version of X-35-02, sharing the same camber and thickness distribution. The aluminum models, with a chord of 400 mm and a span of 1248 mm, which result in a blockage ratio of 11% at 30° angle of attack, were mounted vertically and equipped with 90 and 92 pressure taps, respectively. The geometries of both airfoils are illustrated in Fig. 1.

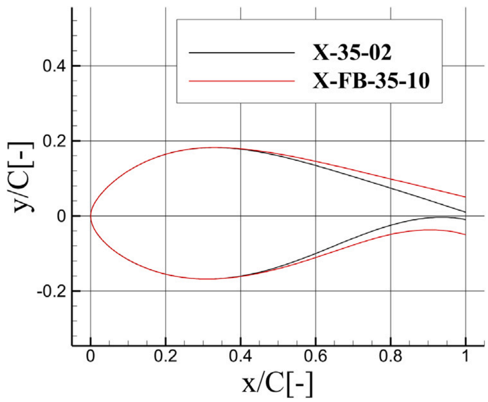

Fig. 1. Cross-sections of the X-35-02 and X-FB-35-10 airfoils.

Table 1
Test matrix of both airfoils in the steady conditions.

Airfoil	Reynolds No. [–]	Transition	VG loc. x/C [–]
X-35-02	1.00E+06	Free	–
X-35-02	1.00E+06	Free	0.3
X-FB-35-10	1.00E+06	Free	–
X-FB-35-10	1.00E+06	Free	0.3

VG strips with counter-rotating vanes, each 5 mm tall, were placed at various chordwise positions on the airfoil's suction side. The vanes were mounted on a 1 mm base plate using 0.05 mm double-sided tape. Vane length, angle, and spacing are unfortunately confidential and cannot be disclosed. A turntable was used for static tests to adjust the angle of attack, while dynamic tests employed an actuator inducing sinusoidal motion about the quarter-chord. The system allowed control of mean angle, amplitude, and frequency. Pitching frequencies of 1, 2, and 3 Hz corresponded to reduced frequencies of 0.032 0.064, and 0.096, enabling varied test conditions. In this study, only the results corresponding to the reduced frequency of 0.064 in the free transition flow regime are considered. A multichannel pressure system recorded surface pressures to compute C_L, C_D, and C_M. A high-speed scanner sampled all ports at 300 Hz and averaged data for static cases. The sampling rate for dynamic measurements involved collecting data for at least 20 cycles, with the dynamic results in this paper representing the averaged values of these cycles.

Since the measured drag coefficient using wake rake leads to enormous error for the separated flows [34], the integrated surface pressure measurement method was employed to calculate drag in both static and dynamic conditions. Moreover, the standard wind tunnel corrections, given by Dalton [35], including the solid and wake blockage and streamline curvature, were applied to the measured data. Phase and amplitude corrections were made using the method given by Bergh and Tijdeman [36] due to the pressure tube length and fluid characteristics in dynamic measurements. The authors in [37] present a detailed unsteady measurement correction approach. The aerodynamic coefficients were calculated using the corrected data and conventional correction methods were applied. Note that the Dalton [35] method is not validated for unsteady measurements.

A test matrix was prepared to investigate various static and dynamic conditions for both airfoils. Both airfoils underwent 16 static and 192 dynamic measurements. Due to space limitations, only selected results are presented in Tables 1 and 2. Full details of the test campaign are available in [37]. The mean angle of attack was fixed at 6°, with two additional angles chosen relative to the stall angle from steady tests: two degrees below the stall (STL–2°) and five degrees above the stall (STL+5°) to represent near-stall conditions.

2.2. Semi-empirical dynamic stall models

In this study two different dynamic stall models has been used. The B-L dynamic stall model developed by Beddoes and Leishman [12] emerged from a series of research projects focused on helicopter aerodynamics. This semi-empirical model has undergone extensive validation against experimental data and is characterized by its relatively low computational complexity, making it suitable for real-time or large-scale simulations. A key advantage of the model lies in its use of static airfoil experimental data to derive the necessary empirical coefficients. This model has been presented and modified in numerous publications over the years, resulting in a variety of formulations tailored to different applications. However, the present study employs the original version of the B-L model, which has been documented in multiple sources, especially with regard to the formulations of the unsteady drag and moment coefficients. For the reader's convenience, the exact formulation implemented in this work is presented in Appendix 6.

The Risø model was developed at Risø National Laboratory in Denmark by Hansen et al. [13] for wind energy applications and is a modified version of B-L model and has therefore the same block structure of the B-L model. This model ignores the compressibility impulsive forces and leading edge separation, due to the low speed flow regimes and thick airfoils application in the wind industry. Considering these assumptions, the attached lift can be obtained by Theodorsen theory and only the trailing edge separation is considered in the stall conditions.

The airfoil-dependent parameters are detailed in Table 3. Note that a piecewise 4th order polynomial curve fitting method was employed to reconstruct the curves from the steady data. The indicial lift and moment response function constants (Ai, bi) for the attached flow part of the models are a function of Mach number [38] and are relatively insensitive to the airfoil shapes, at least for thin airfoils [19]. These constants are determined by fitting the airfoil's harmonic load response (amplitude and phase) obtained from oscillatory tests conducted across various reduced frequencies [39]. For this study, the default values as reported by Beddoes [40] are utilized for both dynamic stall models. These values were computed through a series of CFD simulations at NASA Ames [40] and are used as default values in the aeroelastic codes.

On the other hand, each model is tested using two different configurations of the time constants i.e., T_p and T_f: one with default values and one with adjusted values. In this study, the default values reported by Leishman [41] and Hansen et al. [42] are used for the B-L and Risø models, respectively, representing the state-of-the-art implementations in aeroelastic simulation codes. These constants are presented in Table 4. The leading edge pressure peak time constant, T_p, defines the extent of the linear portion of the lift polar, corresponding to the attached flow phase of the dynamic stall cycle. Consequently, this parameter has a major effect on the maximum lift overshoot (MLOS). According to Leishman [12], T_p is a function of the Mach number and must be determined empirically from unsteady airfoil data. Although T_p is generally considered to be largely independent of airfoil geometry [43], this conclusion primarily applies to thin airfoils. For thick airfoils, separate investigations are necessary to assess the validity of this assumption [41]. However, the boundary layer separation lag time constant, T_f, characterizes the rate at which flow separates from the trailing edge. It defines the angle of attack range over which trailing edge flow separation occurs and primarily influences the dynamic stall angle of attack (DSAOA). Similar to T_p, the parameter T_f is dependent on the Mach number. However, its variation with airfoil geometry is less well understood and more difficult to quantify [12]. The time constants were adjusted with the aim of more accurately reproducing the experimentally observed MLOS and DSAOA.

Note that, due to limitations in the paper length, the results primarily focus on the adjusted parameters, particularly highlighting the B-L model, which is widely utilized in the scientific community. The lift is

Table 2
Test matrix of both airfoils in the dynamic conditions.

Airfoil	Reynolds No. [–]	Transition	VG loc. x/C [–]	Mean AOA α_m [°]	Amplitude A [°]	Frequency fq [Hz]	Reduced frequency k [–]
X-35-02	1.0E+06	Free	–	6°	10°	2	0.064
X-35-02	1.0E+06	Free	–	STL−2°	10°	1,2,3	0.032,0.064,0.096
X-35-02	1.0E+06	Free	–	STL+5°	5°	2	0.064
X-35-02	1.0E+06	Free	0.3	6°	10°	2	0.064
X-35-02	1.0E+06	Free	0.3	STL−2°	10°	2	0.064
X-35-02	1.0E+06	Free	0.3	STL+5°	5°	2	0.064
X-FB-35-10	1.0E+06	Free	–	6°	10°	2	0.064
X-FB-35-10	1.0E+06	Free	–	STL−2°	10°	2	0.064
X-FB-35-10	1.0E+06	Free	–	STL+5°	5°	2	0.064
X-FB-35-10	1.0E+06	Free	0.3	6°	10°	2	0.064
X-FB-35-10	1.0E+06	Free	0.3	STL−2°	10°	2	0.064
X-FB-35-10	1.0E+06	Free	0.3	STL+5°	5°	2	0.064

Table 3
Fixed constants for both dynamic stall models.

Airfoil	VGs [x/C]	$dCN/d\alpha$	$dCL/d\alpha$	α_0	C_{D0}	C_{M0}	η	A_1	b_1	A_2	b_2	A_3	b_3	A_4	b_4	A_5	b_5
X-35-02	–	6.405	6.412	−2.97	0.011	−0.086	0.86	0.3	0.14	0.7	0.53	0.15	0.25	−0.5	0.1	1	0.5
X-35-02	0.3	6.755	6.759	−2.42	0.013	−0.085	0.83	0.3	0.14	0.7	0.53	0.15	0.25	−0.5	0.1	1	0.5
X-FB-35-10	–	7.608	7.660	−3.53	0.040	−0.111	0.75	0.3	0.14	0.7	0.53	0.15	0.25	−0.5	0.1	1	0.5
X-FB-35-10	0.3	7.267	7.294	−3.22	0.039	−0.109	0.73	0.3	0.14	0.7	0.53	0.15	0.25	−0.5	0.1	1	0.5

Table 4
Airfoils, dynamic stall models, and time constants configurations.

Airfoil	VGs [x/C]	Model	Set	T_p	T_f	τ_p	τ_f
X-35-02	–	B-L	Default	1.7	3.0	–	–
X-35-02	–	B-L	Adjusted	0.46	1.93	–	–
X-35-02	–	Risø	Default	–	–	1.5	6.0
X-35-02	–	Risø	Adjusted	–	–	0.4	1.4
X-35-02	0.3	B-L	Default	1.7	3.0	–	–
X-35-02	0.3	B-L	Adjusted	4.89	0.49	–	–
X-35-02	0.3	Risø	Default	–	–	1.5	6.0
X-FB-35-10	–	B-L	Default	1.7	3.0	–	–
X-FB-35-10	–	B-L	Adjusted	1.33	0.01	–	–
X-FB-35-10	–	Risø	Default	–	–	1.5	6.0
X-FB-35-10	0.3	B-L	Default	1.7	3.0	–	–
X-FB-35-10	0.3	B-L	Adjusted	2.74	0.01	–	–
X-FB-35-10	0.3	Risø	Default	–	–	1.5	6.0

the main criterion for adjusting the time constants, which are tuned to match the maximum measured lift overshoot in the dynamic stall cases.

Note that numerous PIV measurements at higher and lower reduced frequencies show no leading edge separation for these airfoils in all configurations during dynamic stall onset. Therefore, the leading edge vortex module is deactivated for the B-L model, and the related parameters, i.e., T_v, T_{vl}, K_{C_T}, D_{C_T}, and C_{N1} are not discussed here. Fig. 2 illustrates the total vorticity contour above both airfoils at the top stagnation angle (TSA), for a reduced frequency of $k = 0.064$ and $\alpha_m = STL - 2°$. The results demonstrate the expansion of the trailing separation towards the leading edge; however, no leading edge separation is visible.

3. Results

The aim of this section is to provide insights into the performance of two dynamic stall models when applied to thick wind turbine airfoils. To investigate this aspect, a series of simulations is carried out using the B-L and Risø models, and the results are compared with the aforementioned experimental data. Three mean angles of attack, namely $\alpha_m = 6°$, $\alpha_m = STL - 2°$, and $\alpha_m = STL + 5°$, representing the linear region, stall, and post-stall phases at a reduced frequency of $k = 0.064$, are chosen to assess the accuracy of the models across different sections of the lift curve. Moreover, two distinct configurations are chosen for each airfoil, one with VGs and one without, under free transition flow regime. To provide more information about the airfoil characteristics, the static polars are shown along with the hysteresis effect.

Fig. 3 illustrates the comparison of the measured steady and dynamic prediction with the B-L and Risø models at various mean angles of attack for the X-35-02 airfoil at a reduced frequency of $k = 0.064$ in the free transition flow regime. At a mean angle of attack of $\alpha_m = 6°$, the measured C_L exhibits a slight deviation in the US and DS-phases compared to the steady polar curve. A minor dynamic stall occurs at the TSA, which is promptly resolved at the onset of the DS-phase. Both the B-L and Risø models accurately predict the cyclic behavior; however, their accuracy diminishes during the DS-phase. Additionally, both models overestimate the MLOS. Note that the tuned B-L model's MLOS is lower than that of default, yet it remains higher than the measured results. At $\alpha_m = STL - 2°$, the measured data reveal the occurrence of a pronounced dynamic stall. It is observed that the dynamic cycle exhibits a higher maximum C_L and a higher stall angle of attack compared to the steady data. Both models demonstrate an elevated MLOS and a faster stall recovery in the DS-phase in comparison to the measurements. The default Risø model displays the highest MLOS and fails to accurately predict the lift reduction, unlike the B-L model. The tuned B-L model accurately represents the MLOS and lift drop; however, its accuracy in stall recovery diminishes. Both models exhibit acceptable accuracy at the conclusion of the DS-phase and the beginning of the US-phase.

The post-stall mean angle of attack (i.e., $\alpha_m = STL + 5°$) leads to the formation of oval-shaped dynamic loops that cycle clockwise, in contrast to the linear segment. The B-L model captures the lift drop and the maximum lift angle of attack more accurately, compared to the Risø model. Moreover, the tuned B-L model better replicates the initiation of the US-phase than the default outcomes.

For drag prediction, the models are unable to accurately replicate the measured data, primarily due to the models' limitations in accurately representing flow separation and reattachment. At $\alpha_m = 6°$ and $\alpha_m = STL - 2°$, the model results match the experimental data in the attached region of the polar, specifically at the beginning of the US-phase. However, significant deviations arise at the onset of dynamic stall and flow separation. Both models fail to predict the maximum drag at the TSA. At $\alpha_m = STL + 5°$, where flow separation occurs on the airfoil, both models underestimate the drag in the US-phase. Note that tuning the B-L model slightly alters the drag cycles, with no significant visible changes.

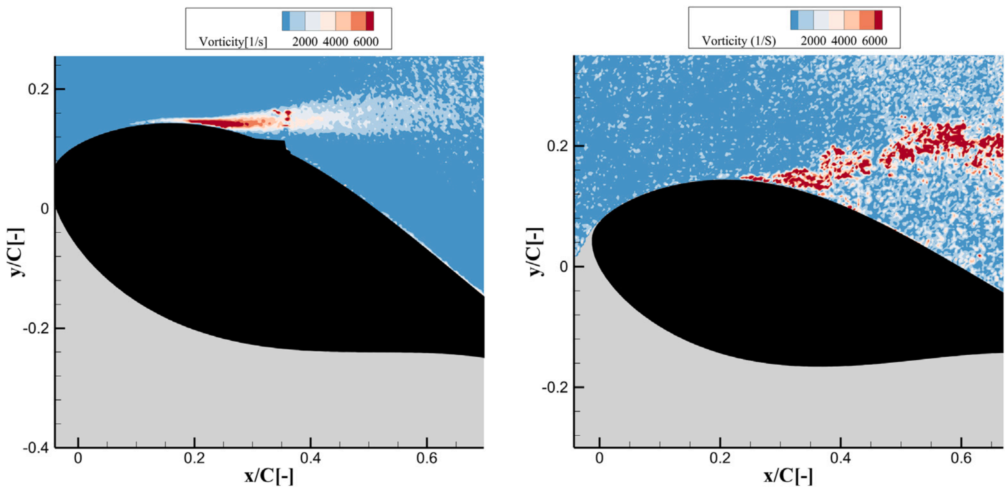

(a) (b)

Fig. 2. Measured total vorticity contour in free transition flow regime [$Re = 1 \times 10^6$, (a): X-FB-35-10, $VGs(x/C) = 0.3$, $A = 10°$, $\alpha_m = STL - 2°$, $\alpha = 30°$, US, phase-averaged, (b): X-35-02, $k = 0.064$, $A = 10°$, $\alpha_m = STL - 2°$, $\alpha = 24°$, US, instantaneous].

As a result of the common issue of flow separation and reattachment modeling, the prediction of the moment coefficient is inaccurate, and the deviation from the measurements amplifies in the flow separation and reattachment phases, namely in the dynamic stall, post-stall, and reattachment segments of the cycles. At $\alpha_m = 6°$, the models can replicate the measured C_M in the lower angles of attack of the cycle but are unable to predict the C_M break angle of attack and magnitude. At $\alpha_m = STL - 2°$ and $\alpha_m = STL{+}5°$, both models fail in predicting the C_M accurately.

The comparison of the dynamic stall models with the measurements at various mean angles of attack for the X-35-02 airfoil with VGs positioned at 30% of the chord length, at a reduced frequency of $k = 0.064$ in the free transition flow regime, is depicted in Fig. 4. At $\alpha_m = 6°$, the models accurately capture the trend of the measurements. However, the deviation of the model results from the measurements increases compared to the configuration without VGs, especially at the TSA and DS-phases. Conversely, the models can predict the maximum and minimum C_L accurately, attributed to the significant distance of the TSA from the stall angle of attack. Additionally, the tuned B-L model exhibits lower accuracy in the US and DS-phases compared to the results from the default.

The results of the models exhibit discrepancies compared to the configuration without VGs at $\alpha_m = STL - 2°$. In this case, the model with default constants underestimates the DSAOA in comparison to the measurements. The B-L model underestimates MLOS and overestimates the magnitude of lift loss. The Risø model accurately predicts the MLOS and the magnitude of lift loss, but the shape of the DS-phase deviates from the measurements. Conversely, the tuned B-L model can predict the MLOS and DSAOA; however, the lift loss deviates from the measurements. All models overpredict the lift in the US-phase and poorly simulate the reattachment phase, particularly the B-L model due to inaccuracies in modeling flow reattachment with VGs. At $\alpha_m = STL{+}5°$, all models exhibit poor prediction of the dynamic cycles in the post-stall region and overestimate the C_L at the bottom stagnation angle (BSA).

At $\alpha_m = 6°$, all models predict the drag cycles in accordance with the measurements; however, they underestimate the maximum and minimum drag coefficient values. The B-L model configurations perform better in predicting the US-phase compared to the Risø model, but both models underpredict DS-phase values. In the dynamic stall cases at $\alpha_m = STL - 2°$, the B-L model configurations demonstrate superior performance to the Risø model and provide a more accurate estimation of the maximum and minimum C_D compared to the measurements. The Risø model exhibits the largest deviation from the measurements at the TSA among the models. At $\alpha_m = STL{+}5°$, the B-L model configurations fail to accurately capture the measured drag cycles and overpredict the maximum C_D at the TSA. In contrast, the Risø model accurately predicts the maximum and minimum drag coefficients but struggles to replicate the measured post-stall cycle correctly. Note the tuned B-L model minimally alters the drag cycles. Owing to the previously discussed issue, the moment cycle predictions and C_M break points cannot be accurately predicted, leading to the models' failure in predicting the maximum and minimum C_M values and angles of attack accurately at $\alpha_m = STL - 2°$ and $\alpha_m = STL{+}5°$. Only at $\alpha_m = 6°$, i.e., linear part of the lift curve, the models correctly capture the cycle form.

Fig. 5 depicts the comparison between the measured steady and dynamic data and the dynamic stall models at different mean angles of attack for the X-FB-35-10 flatback airfoil at a reduced frequency of $k = 0.064$ in the free transition flow regime. At $\alpha_m = 6°$, the dynamic stall models reproduce the trend of the measurements, but overpredict the maximum C_L. However, the inaccuracy increases to half at the top and bottom of the US and DS-phases respectively. Furthermore, the tuned B-L model demonstrates a more accurate prediction of the maximum C_L at the TSA compared to the measurements. At $\alpha_m = STL - 2°$, both models overpredict the MLOS and slightly underpredict the DSAOA. Additionally, both configurations of the B-L model overpredict the lift decrease after the stall, unlike the Risø model. The tuned B-L model accurately predicts the MLOS, but the predicted DSAOA is slightly lower than the measurements. Unfortunately, it is not feasible to adjust both values simultaneously. All dynamic stall models fail to accurately model flow reattachment in the DS-phase, with increased inaccuracy observed in the tuned B-L model. At $\alpha_m = STL{+}5°$, the Risø model overpredicts the C_L at the BSA, whereas the B-L model configurations exhibit improved C_L at the BSA.

For drag prediction, at $\alpha_m = 6°$, the B-L model configurations overpredict the drag magnitude in both the US and DS-phases, particularly at the TSA. The Risø model more accurately predicts the maximum C_D compared to the B-L model, but it underestimates the C_D at the top and bottom parts of the US and DS-phases, respectively. Once again, due to flow separation modeling issues, both models fail to accurately capture the drag cycles at $\alpha_m = STL - 2°$ and $\alpha_m = STL{+}5°$. Note that the B-L model overpredicts the magnitude of C_D, which is attributed not only to the inaccuracy of flow separation/reattachment modeling but also to the C_T calculation in separated flow, which is based on C_N.

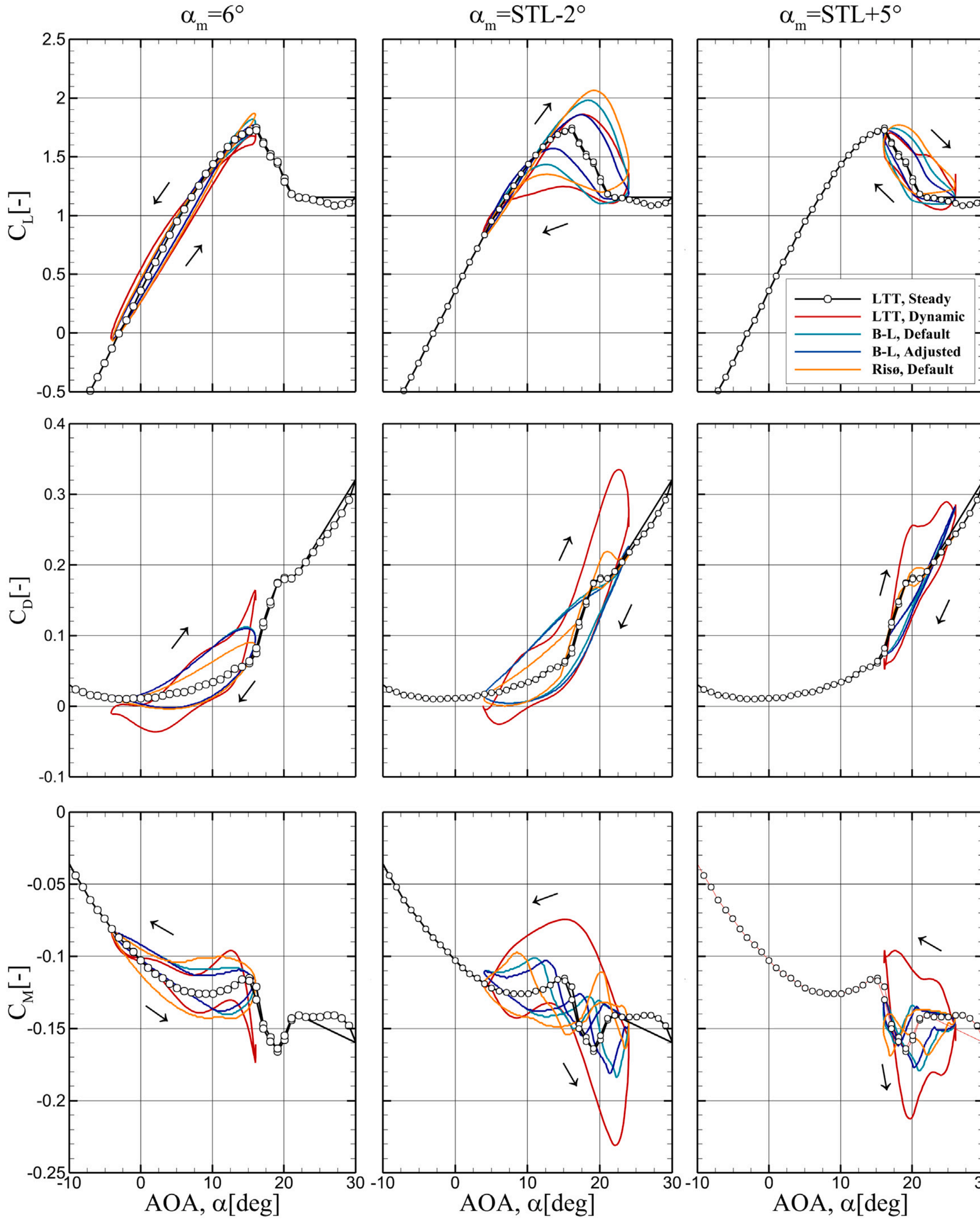

Fig. 3. Measured and simulated dynamic polars in free transition flow regime [$Re = 1 \times 10^6$, X-35-02, $k = 0.064$].

Similar to previous observations, the models accurately capture the cycle form only during attached flow, but they fail to predict the shape, C_M break point, and the maximum and minimum C_M angles of attack.

The comparison between the dynamic stall models and the measurements at different mean angles of attack for the X-FB-35-10 airfoil with VGs positioned at 30% of the chord length, at a reduced frequency of $k = 0.064$ in the free transition flow regime, is illustrated in Fig. 6.

At $\alpha_m = 6°$, the TSA remains well below the steady stall angle of attack, and a similar trend to the configuration without VGs can be observed in the dynamic cycles of the C_L. Both dynamic stall models overestimate the magnitude of the MLOS at $\alpha_m = STL - 2°$, with the Risø model showing a particularly pronounced overestimation. Furthermore, the DSAOA predicted by the B–L model is slightly lower than the experimental measurements. The tuned B-L model was only adjusted to match the MLOS value and not the DSAOA simultaneously, resulting in a larger discrepancy compared to the tuned model without VGs. Both models overpredict the lift fall during stall, and the accuracy of the tuned B-L model is reduced during the DS-phase, compared to the measurements. At $\alpha_m = STL+5°$, all models exhibit an overestimation of the lift coefficient at the BSA and demonstrate a higher LFR than observed in the measurements.

For the prediction of drag and pitching moment of the airfoil equipped with VGs, a similar behavior to the configuration without VGs is observed. Specifically, the models fail to capture the trends observed in the measurements, as well as the maximum and minimum values of the dynamic cycles at $\alpha_m = STL - 2°$ and $\alpha_m = STL+5°$, primarily

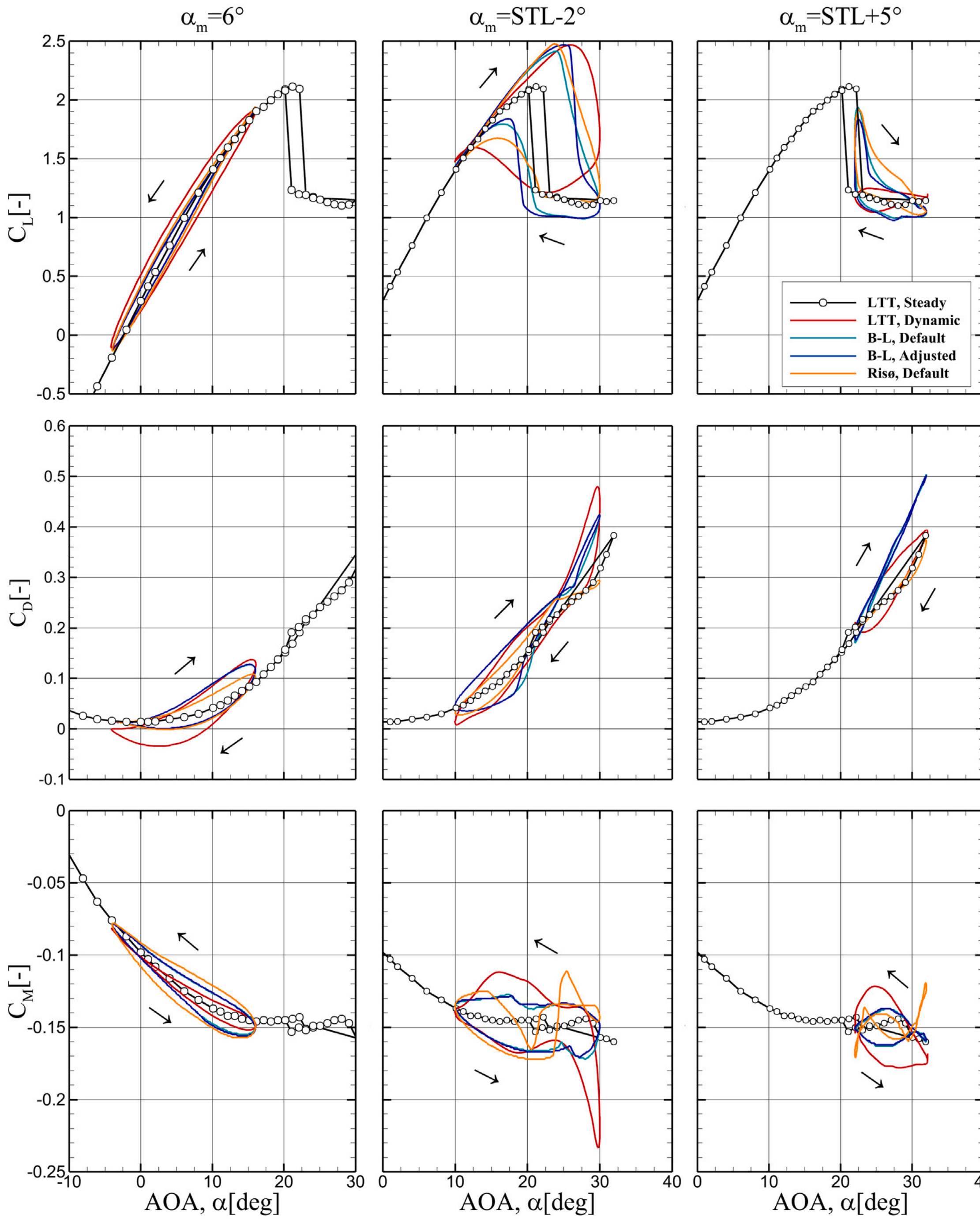

Fig. 4. Measured and simulated dynamic polars in free transition flow regime [$Re = 1 \times 10^6$, X-35-02, $k = 0.064$, $VGs(x/C) = 0.3$].

due to inaccuracies in modeling the flow separation and reattachment phases.

Fig. 7 depicts the comparison between the dynamic stall models with default constants and the tuned Risø model at $\alpha_m = STL - 2°$ for the X-35-02 airfoil. Note that the adjusted Risø model accurately predicts the MLOS and DSAOA in the C_L cycles. However, this adjustment leads to premature flow reattachment in the DS-phase, similar to the behavior observed with the B-L model. The tuned Risø model exhibits slight discrepancies in dynamic drag prediction compared to the default constants and fails to predict the cycle form and the DFR, which is also evident in the C_M cycle prediction, where the tuned Risø model shows no enhancements over the default constants.

Figs. 8 and 9 show the comparative performance of both dynamic stall models for the X-35-02 airfoil under free-transition flow conditions at a mean angle of attack of $\alpha_m = STL - 2$. The results correspond to reduced frequencies of $k = 0.032$ and $k = 0.096$, respectively, while employing the time constants previously adjusted for $k = 0.064$. Although these constants were originally calibrated for a mid-range reduced frequency, the adjusted models exhibit satisfactory predictive capability for the MLOS across both lower and higher reduced frequencies. This indicates a degree of robustness in the parameter tuning beyond the calibration point. In contrast, models using default constants demonstrate substantial inaccuracies, particularly in estimating the MLOS and the DSAOA. Furthermore, consistent with earlier observations, neither

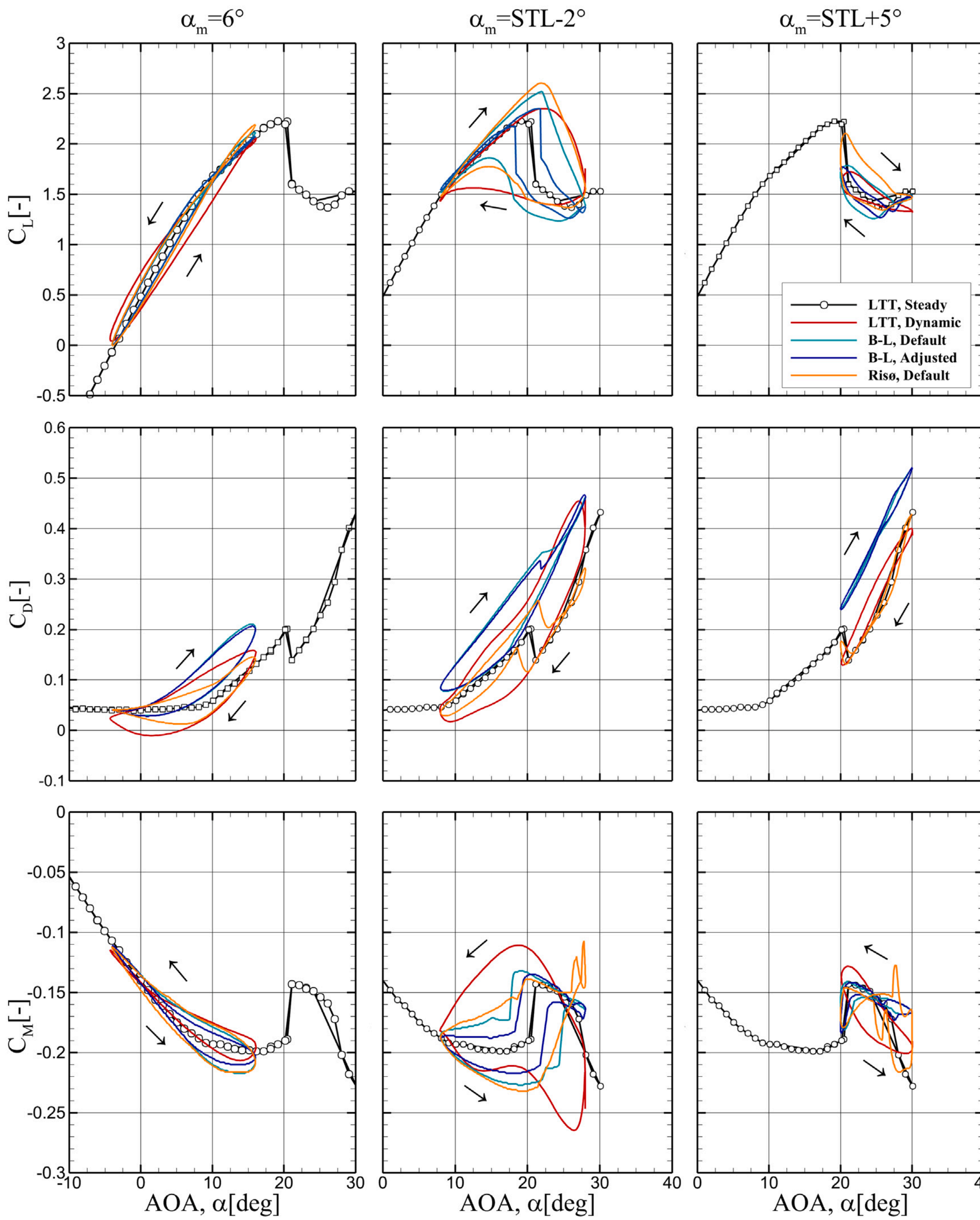

Fig. 5. Measured and simulated dynamic polars in free transition flow regime [$Re = 1 \times 10^6$, X-FB-35-10, $k = 0.064$].

model successfully captures the dynamic evolution of dynamic C_D and C_M throughout the stall cycle.

A comparison with previous attempts to calibrate the Beddoes–Leishman (B-L) model reveals a clear trend. The adjustments performed by Melani et al. [22] for the NACA0012 airfoil demonstrate that the B-L model achieves good agreement with experimental data in both attached and separated flow regimes, i.e., during dynamic stall and post-stall conditions. The DSAOA, along with the characteristic increase in drag and pitching moment, is well captured by the model, confirming the validity of the Beddoes stall criterion for this class of airfoils. However, when the airfoil thickness increases to 21% (S809 airfoil), the model exhibits reduced calibration capability, particularly for unsteady drag and pitching moment coefficients. Despite this limitation, the inaccuracies in drag and pitching moment predictions remain smaller than those observed in the present study, and the peak angle of attack for these quantities is still predicted correctly. It should be noted that for both airfoils examined in the previous studies, the LEV module was active, unlike in the current investigation. Furthermore, differences in reduced frequency, mean angle of attack, and Reynolds number between the previous studies and the present work preclude a direct quantitative comparison. Therefore, only qualitative trends in the results can be meaningfully assessed.

Figs. 10 and 11 present the percentage error between the calculated and measured maximum values for key aerodynamic coefficients at different mean angles of attack and reduced frequencies respectively. These coefficients play a vital role in aeroelasticity and aerodynamic

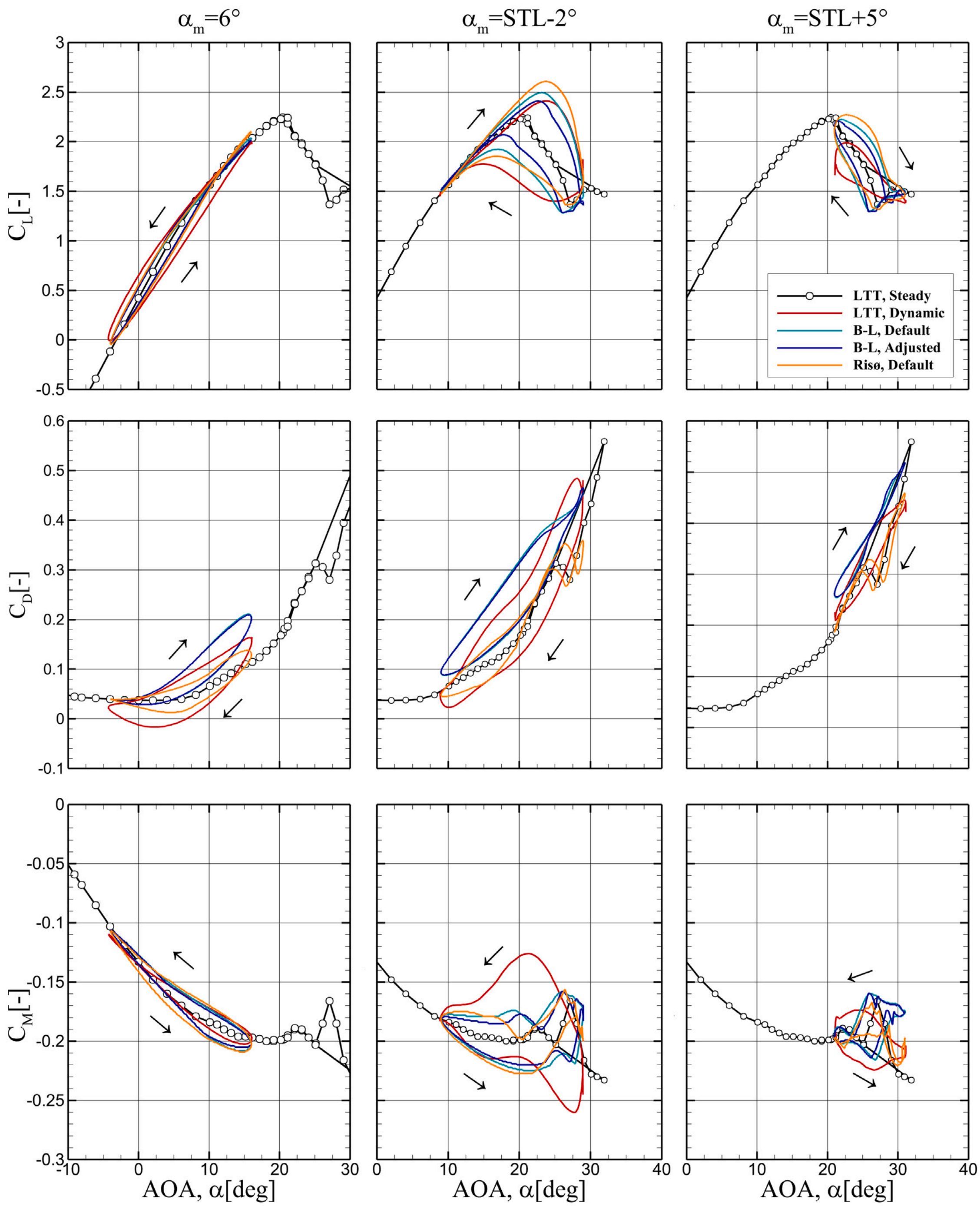

Fig. 6. Measured and simulated dynamic polars in free transition flow regime [$Re = 1 \times 10^6$, X-FB-35-10, $k = 0.064$, $VGs(x/C) = 0.3$].

load calculations, which are essential for determining the structural integrity and dynamic behavior of the blades. Any discrepancy between the calculated and measured values directly influences the reliability of load estimations. A significant error observed in these coefficients, such as 11% for C_{L-max} and 28% for C_{M-max} at $\alpha_m = STL - 2°$, provide a quantitative representation of the uncertainty in the load calculation process, using default time constants in the models. Note no improvements is seen in the C_{M-max} and C_{D-max} for the adjusted B-L model. Furthermore, the results indicate that an increase in reduced frequency leads to a greater error in predicting the maximum aerodynamic coefficients for both models. This underscores the importance of implementing refined modeling approaches or improved measurement techniques to enhance predictive accuracy. Note that the normalized mean absolute error (NMAE) of all predictions are shown in Appendix 7.

3.1. Discussion

The inaccuracy in modeling dynamic stall for thick airfoils is primarily attributed to the treatment of the trailing edge module in both models. Trailing edge flow separation leads to a loss of circulation and introduces nonlinear behavior in the lift, drag, and pitching moment characteristics. Both dynamic stall models employ the Kirchhoff/Helmholtz formulation [38], originally developed to model lift on a flat plate, to simulate the nonlinear effects of trailing edge separation on lift. This approach yields reasonable results for thin airfoils, where

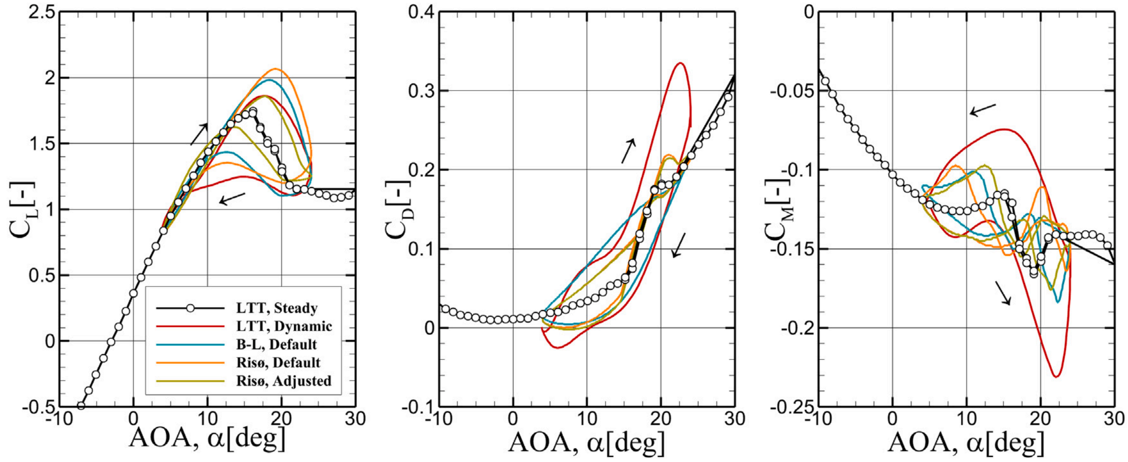

Fig. 7. Measured and simulated dynamic polars in free transition flow regime [$Re = 1 \times 10^6$, X-35-02, $k = 0.064$].

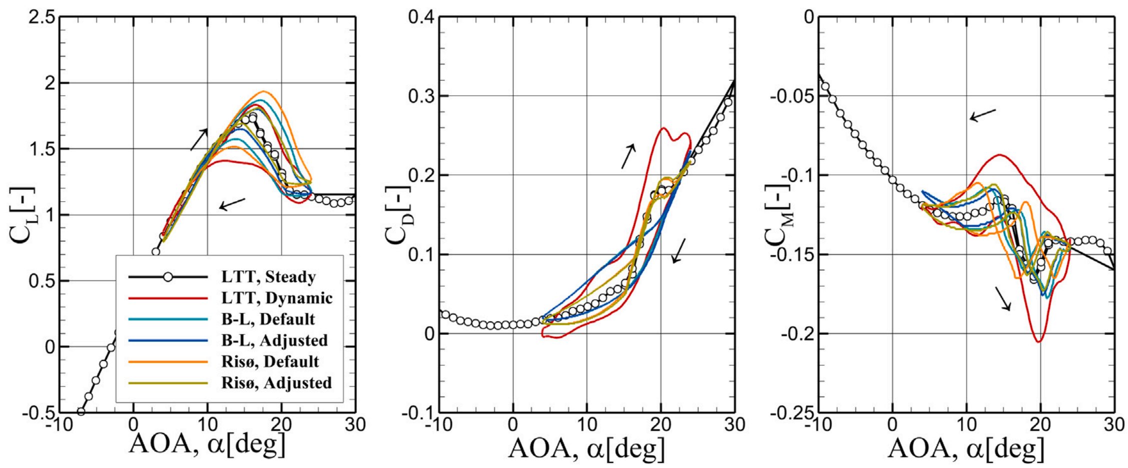

Fig. 8. Measured and simulated dynamic polars in free transition flow regime [$Re = 1 \times 10^6$, X-35-02, $k = 0.032$].

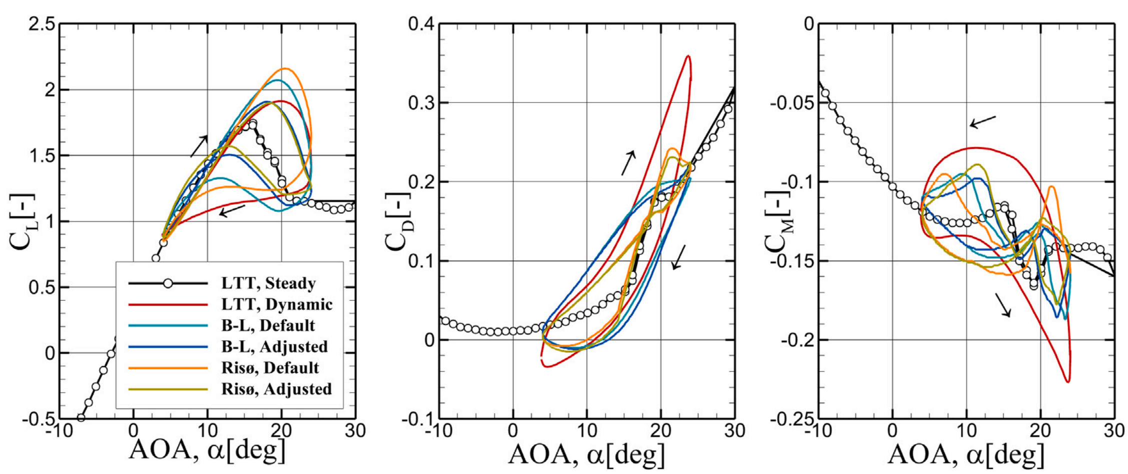

Fig. 9. Measured and simulated dynamic polars in free transition flow regime [$Re = 1 \times 10^6$, X-35-02, $k = 0.096$].

the stall mechanism typically involves a combination of progressive trailing edge separation and abrupt leading edge stall as the angle of attack increases [44]. For such airfoils, the angle of attack range associated with trailing edge separation is relatively narrow, and the leading edge separation occurs at comparatively low angles of attack [45]. The B-L and Risø models are based on this flow separation mechanism. In these models, the leading edge vortex (LEV), which is responsible for the peak values in C_L and C_M, is triggered shortly after trailing edge separation. This results in good agreement with experimental measurements for thin airfoils.

In contrast to thin airfoils, thick airfoils exhibit a fundamentally different flow separation mechanism, which alters the nonlinear lift behavior. These airfoils experience a stronger adverse pressure gradient on the suction side compared to thinner airfoils. Moreover, the LEV

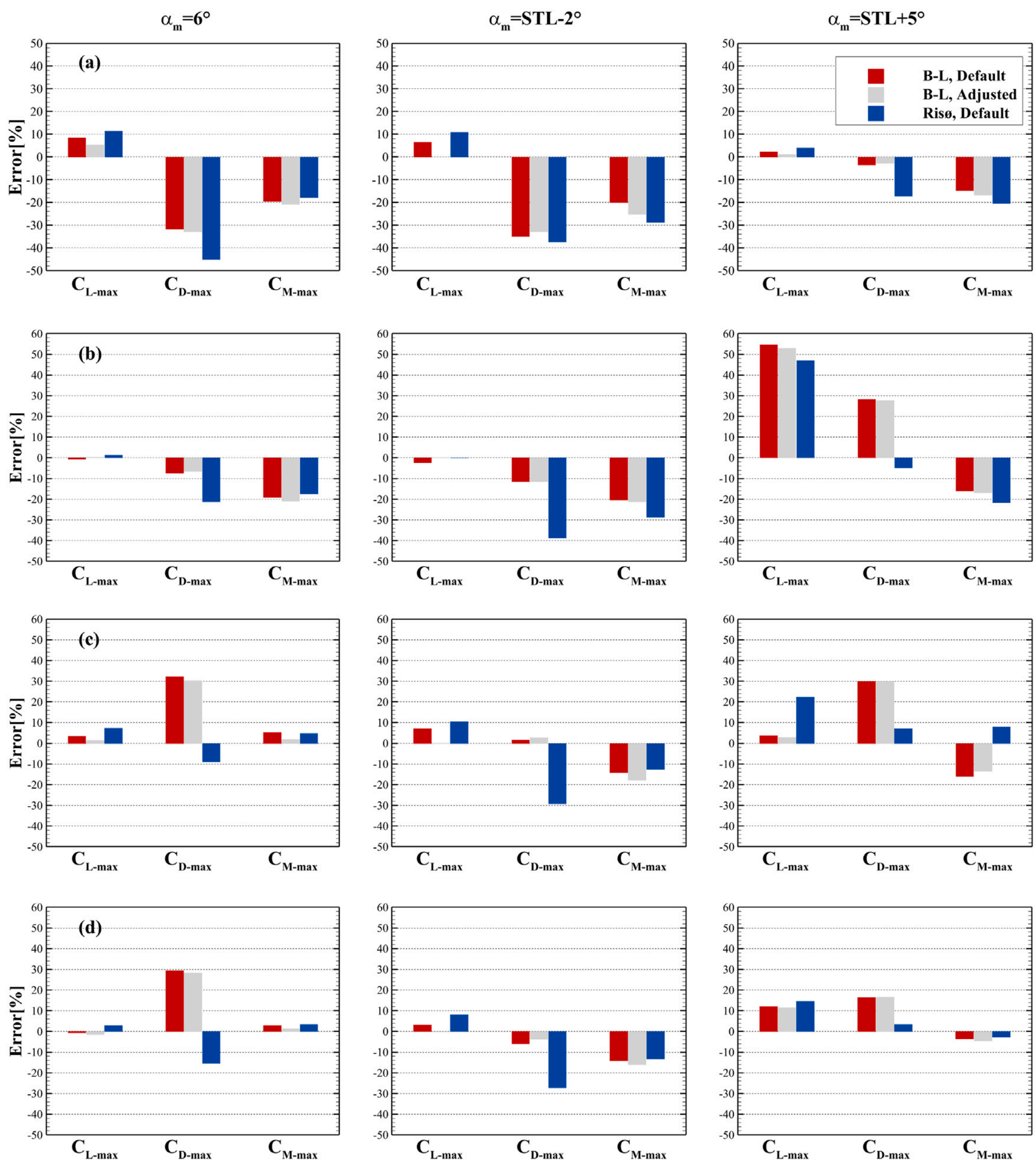

Fig. 10. Variation in error of maximum aerodynamic coefficients across different airfoils at various mean angles of attack [$Re = 1 \times 10^6$, (a) X-35-02, (b) X-35-02, $VGs(x/C) = 0.3$, (c) X-FB-35-10, (d) X-FB-35-10, $k = 0.064$, $VGs(x/C) = 0.3$].

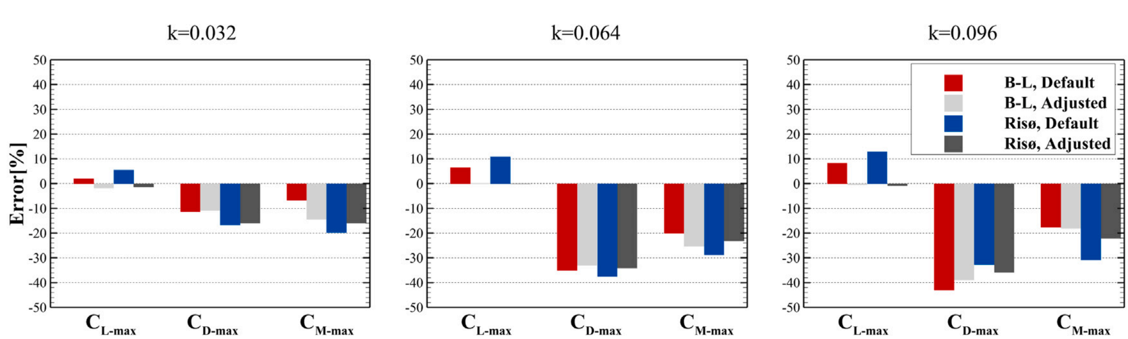

Fig. 11. Variation in error of maximum aerodynamic coefficients for different reduced frequencies in free transition flow [$Re = 1 \times 10^6$, X-35-02, $\alpha_m = STL-2°$].

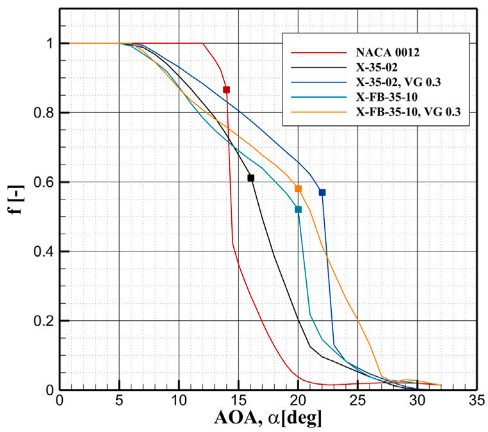

Fig. 12. Comparison of the calculated effective separation point distribution for different airfoils.

forms at significantly higher angles of attack (higher from the range of this study), while the trailing edge separation plays a dominant role in shaping the lift nonlinearities prior to stall onset [46]. For thick airfoils, trailing edge separation is a gradual process that initiates at relatively lower angles of attack than in thin airfoils. As the angle of attack increases, the separated flow region slowly progresses toward the leading edge but remains confined behind the location of maximum airfoil thickness over a range of angles. This behavior has been observed by the authors through CFD and PIV measurements, with detailed results to be presented in a forthcoming publication. The flow separation dynamics of flatback airfoils are even more complex than those of conventional thick airfoils. These airfoils exhibit multiple vortical structures that originate at the trailing edge and along the suction surface. At post-stall angles of attack, these vortices merge, significantly altering the pressure distribution around the airfoil. Additionally, the VGs introduce a secondary vortical system oriented perpendicular to the primary one, further enhancing the flow nonlinearities. Consequently, the application of Kirchhoff's theory alone is insufficient to accurately model the complex flow structures associated with thick and flatback airfoils.

The comparison of the calculated effective separation point distribution, based on the Kirchhoff formulation for a NACA 0012 thin airfoil [47] and the thick airfoils studied in this research, is presented in Fig. 12. The steady stall angle of attack is indicated on each curve as a square. Note that the B-L model demonstrates good agreement with the dynamic measurements in various phases of dynamic stall [12], contrasting the presented results. The disparity between the calculated separation points for thin and thick airfoils is clearly visible. As previously mentioned, the NACA 0012 airfoil exhibits a short trailing edge separation phase (2°) until reaching the steady stall angle of attack, followed by a short phase (0.2°) at f = 0.7, which is used to determine the critical angle of attack for triggering the LEV module [12]. Conversely, trailing edge separation for thicker airfoils initiates at much lower angles of attack, and a significant portion of the separation point curve is utilized to predict the dynamic stall and reattachment phases of the cycle.

Future studies may focus on refining the leading edge pressure peak concept, originally proposed by Beddoes [48], which serves as a criterion to link flow separation to the maximum suction peak near the leading edge (see Eqs. (24)–(30)). In this approach, Beddoes introduced a lagged normal force coefficient, C'_N, which is used to compute an equivalent lagged angle of attack. This lagged angle is then employed to determine the dynamic separation point f_{bl}. Each of these steps is currently modeled using a first-order lag formulation. However, first-order lag models are limited in their ability to capture multiple time scales and the nonlinear behavior of vortex dynamics during separation and reattachment, particularly for thick airfoils. Replacing them with higher-order formulations could potentially improve model fidelity. Additionally, the normal force coefficient C_N^P in Eq. (24) could be corrected at higher angles of attack to better account for strong nonlinearities via additional term in the equation. Enhancing the formulation of f_{bl} may also lead to improved predictions of the pitching moment coefficient C_M during the trailing edge separation phase. Additionally, a novel approach is necessary for the B-L model to predict C_T that is not solely reliant on the C_N. Further investigations could explore the development of a new trailing edge separation model specifically tailored to the flow separation characteristics of thick airfoils, as a replacement for the Kirchhoff/Helmholtz-based approach (Eq. (23)). Emerging machine learning techniques may also be leveraged to enhance this new formulation, provided that sufficient wind tunnel measurement data is available for training and validation. These proposed improvements are equally applicable to the Risø model, which employs a similar trailing edge separation framework.

4. Conclusions

The objective of this study is to investigate the accuracy of dynamic stall models on thick wind turbine airfoils equipped with VGs. To achieve this goal, a set of experiments was carried out in the LTT wind tunnel at TU Delft. Two distinct airfoils, X-35-02 and X-FB-35-10, were examined across various mean angles of attack, reduced frequencies, and VGs chord position. Aerodynamic coefficients were determined using surface pressure measurements and the results were compared to the B-L and Risø dynamic stall models. Since the PIV measurements shown no LEV in different airfoil configurations and test conditions, this module was disabled for the B-L model.

The simulated lift cycles indicate that the models correctly predict the cycle direction. However, the discrepancy between the models and the measurements becomes more pronounced as the size of flow separation above the airfoil increases. This discrepancy is attributed to the lack of accuracy in the trailing edge separation/reattachment modeling within the models. Particularly, this discrepancy is more evident for the $\alpha_m = STL - 2°$ cases, where flow separation and reattachment occur during the US and DS-phases. This modeling inaccuracy leads to incorrect values for MLOS, DSAOA, post-stall lift drop, and lift in the DS-phase of a dynamic stall event. The same behavior is observed at both higher and lower reduced frequencies. Since the Risø model is based on the B-L model, similar discrepancies are observed in the predictions of both models. Notably, no significant difference in lift cycle prediction accuracy is observed between flatback and non-flatback airfoils.

The results indicate that models using default time constants tend to overpredict the MLOS magnitude, resulting in an overestimation of the load simulation on the rotor blade. Conversely, this inaccuracy is mitigated in the cases involving VGs. This behavior may be linked to the specific combination of VGs position and airfoil, requiring further investigation. Additionally, the time constants T_p and T_f can be utilized to adjust MLOS in dynamic stall models; however, this adjustment compromises the accuracy of reattachment in the DS-phase for both airfoils. Additionally, adjustments can be made to either the MLOS or the DSAOA, but not both simultaneously. This characteristic of model adjustment is also evident in the Risø model. Note that modifications to the indicial lift and moment function constants (A_i, b_i) primarily influence the attached-flow portion of the dynamic stall cycle. Adjusting these parameters does not improve the accuracy of the model in predicting separated flow behavior. However, due to limited knowledge of their dependence on airfoil geometry, a study on the influence of airfoil thickness on these coefficients is recommended.

In general, both models fail to accurately predict the C_D and C_M. Adjusting the MLOS has minimal impact on these cycles. The Risø model utilizes steady drag to compute the dynamic C_D, resulting in more precise DFR in the post-stall region compared to the B-L model.

However, the Risø model still struggles to accurately predict the magnitude of the cycles. The B-L model's dynamic C_D prediction for the flatback airfoil exhibits greater inaccuracy than for the X-35-02 airfoil, as the flatback airfoils have higher steady drag than conventional airfoils. The B-L model's drag prediction method is based on the coefficient of normal force, hence this inaccuracy is expected. Similar inaccuracies in dynamic C_D predictions are observed for the X-35-02 airfoil with VGs. The predicted dynamic C_M cycles align with the measured trends and cycle directions when no trailing edge separation occurs for both airfoils and various configurations. However, in cases of flow separation, the models fail to capture the measured cycle trends and magnitudes.

This research reveals the notably poor predictive performance of the B-L and Risø dynamic stall models in capturing the unsteady aerodynamic behavior of thick conventional and flatback airfoils, both with and without VGs. These findings highlight significant limitations in the accuracy and reliability of dynamic load prediction and aeroelastic analysis for modern large wind turbines when using current dynamic stall models, particularly those employing default time constants. While the accuracy of the MLOS is adjustable, the post-stall lift drop, DS lift, C_D, and C_M remain inaccurately predicted. Given the widespread implementation of these models in scientific and industry-standard aeroelastic simulation tools such as HAWC2, OpenFAST, and Bladed, their inaccuracies introduce significant uncertainty into aeroelastic predictions of the aerodynamic loads and structural responses. This study encourages further development of new separation/reattachment modules specifically tailored for thick airfoils within the existing dynamic stall models. A more precise trailing edge separation module is likely to enhance the accuracy of C_D and C_M predictions. Additionally, a novel approach is necessary for the B-L model to predict C_T that is not solely reliant on the C_N.

CRediT authorship contribution statement

Mehdi Doosttalab: Writing – review & editing, Writing – original draft, Visualization, Validation, Software, Methodology, Investigation, Formal analysis, Data curation, Conceptualization. **Carlos Simão Ferreira:** Supervision. **Daniele Ragni:** Supervision. **Wei Yu:** Supervision. **Christof Rautmann:** Project administration, Funding acquisition.

Declaration of competing interest

The authors declare the following financial interests/personal relationships which may be considered as potential competing interests: Mehdi Doosttalab reports financial support was provided by Nordex Energy GmbH. Mehdi Doosttalab reports a relationship with Nordex Energy GmbH that includes: employment. If there are other authors, they declare that they have no known competing financial interests or personal relationships that could have appeared to influence the work reported in this paper.

Acknowledgments

This work was funded by Nordex Energy SE & Co. KG and the authors are very grateful for this support.

Appendix 6

This appendix provides a detailed presentation of the mathematical formulations underlying the B-L dynamic stall model implemented in this study. These formulations are provided by Beddoes [40], Leishman [49], Beddoes and Leishman [12], Melani et al. [22], and Pereira et al. [4].

6.1. Unsteady attached flow

The total normal force coefficient can be calculated as:

$$C^P_{N_{(s)}} = C^C_{N_{(s)}} + C^I_{N_{(s)}} \tag{1}$$

where the $C^C_{N_{(s)}}$ and $C^I_{N_{(s)}}$ are the circulatory and noncirculatory normal force coefficient respectively and s is obtained by:

$$s = \frac{2V\ t}{C} \tag{2}$$

$$C^C_{N_{(s)}} = \frac{dC_N}{d\alpha}(\alpha_{qs(0)}\phi_{(s)} + \int_0^s \frac{\alpha_{qs}}{dt}\phi_{(s-\sigma)}d\sigma - \alpha_0) \tag{3}$$

$$\phi_{(s)} = 1 - A_1 e^{-b_1\beta^2 s} - A_2 e^{-b_2\beta^2 s} \tag{4}$$

where $A_1 = 0.165$, $A_2 = 0.335$, $b_1 = 0.045$, $b_2 = 0.3$ are the constants for the flat plate and $\beta = \sqrt{1-M^2}$ is the compressibility factor.

$$C^C_{N_{(s)}} = \frac{dC_N}{d\alpha}(\alpha_{e(s)} - \alpha_0) \tag{5}$$

$$\alpha_{e(s)} = \alpha_{qs(s)} - X^1_{(s)} - X^2_{(s)} \tag{6}$$

$$\alpha_{qs} = (\alpha + \frac{C}{2V}\frac{d\alpha}{dt}) \tag{7}$$

and

$$X^1_{(s)} = X^1_{(s-\Delta s)}e^{\left(-b_1\beta^2\Delta s\right)} + A_1\Delta_{qs(s)}e^{\left(-b_1\beta^2\frac{\Delta s}{2}\right)} \tag{8}$$

$$X^2_{(s)} = X^2_{(s-\Delta s)}e^{\left(-b_2\beta^2\Delta s\right)} + A_2\Delta_{qs(s)}e^{\left(-b_2\beta^2\frac{\Delta s}{2}\right)} \tag{9}$$

where $\Delta s = s_n - s_{n-1} = {}^{2V}/_{C}\left(t_n - t_{n-1}\right)$ and $\Delta\alpha_{qs(s)} = \alpha_{qs(s)} - \alpha_{qs(s-1)}$

$$C^I_{N_{(s)}} = \frac{4K_\alpha T_I}{M}\left(\frac{\Delta\alpha_{qs(t)}}{\Delta t} - D_{(t)}\right) \tag{10}$$

where:
$T_I = MC/V$
$K_\alpha = 0.75$
$\Delta t = t_n - t_{n-1}$

$$D_{(t)} = D_{(t-\Delta t)}e^{\left(\frac{-\Delta t}{K_\alpha T_I}\right)} + \left(\frac{\Delta\alpha_{qs(t)}}{\Delta t} - \frac{\Delta\alpha_{qs(t-\Delta t)}}{\Delta t}\right)e^{\left(\frac{-\Delta t}{2K_\alpha T_I}\right)} \tag{11}$$

The tangential force coefficient can be calculated as:

$$C^P_{T_{(s)}} = \frac{dC_N}{d\alpha}(\alpha_{e(s)} - \alpha_0)tan\alpha_{e(s)} \tag{12}$$

The same approach of normal force coefficient can be used to calculate the pitching moment coefficient. The circulatory pitching moment coefficient is obtained by:

$$C^C_{M_{(s)}} = -\frac{dC_N}{16\ d\alpha}(q_{(s)} - X^3_{(s)}) \tag{13}$$

$$X^3_{(s)} = X^3_{(s-\Delta s)}e^{\left(-b_5\beta^2\Delta s\right)} + A_5\Delta q_{(s)}e^{\left(-b_5\beta^2\frac{\Delta s}{2}\right)} \tag{14}$$

$$q = \frac{C}{V}\frac{d\alpha}{dt} \tag{15}$$

$$C^I_{M,\alpha_{(s)}} = -\frac{1}{M}\frac{T_I}{2M}\left[A_3 b_3 T_{\alpha,M}\left(\frac{d\alpha_{(s)}}{dt} - X^4_{(s)}\right) + A_4 b_4 T_{\alpha,M}\left(\frac{d\alpha_{(s)}}{dt} - Y^4_{(s)}\right)\right] \tag{16}$$

$$X^4_{(s)} = X^4_{(s-\Delta s)}e^{-\left(\frac{\Delta s}{b_3 T_{\alpha,M}}\right)} + \left(\frac{d\alpha_{(s)}}{dt} - \frac{d\alpha_{(s-\Delta s)}}{dt}\right)e^{-\left(\frac{\Delta s}{2b_3 T_{\alpha,M}}\right)} \tag{17}$$

$$Y^4_{(s)} = Y^4_{(s-\Delta s)}e^{-\left(\frac{\Delta s}{b_4 T_{\alpha,M}}\right)} + \left(\frac{d\alpha_{(s)}}{dt} - \frac{d\alpha_{(s-\Delta s)}}{dt}\right)e^{-\left(\frac{\Delta s}{2b_4 T_{\alpha,M}}\right)} \tag{18}$$

$$T_{\alpha,M} = \frac{(A_3 b_4 + A_4 b_3)2M}{b_3 b_4 (1-M)} \tag{19}$$

$$C^I_{M,q_{(s)}} = -\frac{7T_{q,M}}{12M}\frac{T_I}{2M}\left(\frac{dq_{(s)}}{dt} - D^1_{M,q(S)}\right) \tag{20}$$

$$D^1_{M,q(S)} = D^1_{M,q(s-\Delta s)} e^{-\left(\frac{\Delta s}{T_{q,M}}\right)} + \left(\frac{dq_{(s)}}{dt} - \frac{dq_{(s-\Delta s)}}{dt}\right) e^{-\left(\frac{\Delta s}{2T_{q,M}}\right)} \tag{21}$$

$$T_{q,M} = \frac{14M}{15(1-M) + 1.5\beta^2 M^2 A_5 b_5 \frac{dC_N}{d\alpha}} \tag{22}$$

6.2. Unsteady non-linear trailing edge separated flow

To account for lift-slope loss from trailing-edge separation, the model uses Kirchhoff–Helmholtz theory for a flat plate. It depends on angle of attack, attached-flow lift slope, and the separation point location (f) on the airfoil. The nonlinear normal force coefficient for separated trailing-edge flow is:

$$C^{st}_N = \frac{dC_N}{d\alpha}\left(\frac{1+\sqrt{f}}{2}\right)^2 (\alpha - \alpha_0) \tag{23}$$

The leading edge pressure lag is calculated as follows:

$$C'_N = C^P_{N_{(s)}} - D_{pf(s)} \tag{24}$$

$$D_{pf(s)} = D_{pf(s-\Delta s)} e^{\frac{-\Delta s}{T_p}} + \left(C^P_{N_{(s)}} - C^P_{N_{(s-\Delta s)}}\right) e^{\frac{-\Delta s}{2T_p}} \tag{25}$$

To consider the effect of the boundary layer response lag, a second separation position function is defined as:

$$f_{bl} = f_p - D_{bl} \tag{26}$$

$$f_p = f_{(\alpha_f)} \tag{27}$$

$$\alpha_f = \frac{C'_N}{\frac{dC_N}{d\alpha}} + \alpha_0 \tag{28}$$

$$D_{bl(s)} = D_{bl(s-\Delta s)} e^{\frac{-\Delta s}{T_f}} + \left(f_{p(s)} - f_{p(s-\Delta s)}\right) e^{\frac{-\Delta s}{2T_f}} \tag{29}$$

The nonlinear normal force coefficient, considering the trailing edge separation is determined by:

$$C^f_{N_{(s)}} = \frac{dC_N}{d\alpha}\left(\frac{1+\sqrt{f_{bl}}}{2}\right)^2 \left(\alpha_{e(s)} - \alpha_0\right) + C^I_{N_{(s)}} \tag{30}$$

The tangential force and pitching moment coefficients are calculated by:

$$C^f_{T_{(s)}} = \eta C^P_{T_{(s)}} \sqrt{f_{bl}} \tag{31}$$

$$C^f_{M_{(s)}} = C^f_{N_{(s)}} X_{CP.N(s)}\left(f_{bl}\right) \tag{32}$$

where X_{CP} is the center of pressure offset from the quarter-chord, expressed as a function of trailing-edge separation $X_{CP} = f(f_{sep})$, and calculated from static airfoil polars by:

$$X_{CP.N}(\alpha) = \frac{C^{st}_M - C_{M0}}{C^{st}_N} \tag{33}$$

6.3. Leading edge separation or dynamic stall onset

The vortex shedding normal force is obtained by:

$$C^v_{N_{(s)}} = \begin{cases} C_{v(s-\Delta s)} e^{\frac{-\Delta s}{T_v}} + \left(C_{v(s)} - C_{v(s-\Delta s)}\right) e^{\frac{-\Delta s}{2T_v}};\ 0 < \tau_{v(s)} < T_{vl} \\ C_{v(s-\Delta s)} e^{\frac{-\Delta s}{T_v}} \qquad ;\ else \end{cases} \tag{34}$$

$$C_{v(s)} = C^P_{N_{(s)}}\left(1 - \left(\frac{1+\sqrt{f_{bl}}}{2}\right)^2\right) \tag{35}$$

$$\tau_{v(s)} = \begin{cases} \tau_{v(s-\Delta s)} + 0.45\Delta s \ ;\ C^f_{N_{(s)}} > C_{N1} \\ 0.0 \ ;\ C^f_{N_{(s)}} < C_{N1} \ and\ \Delta\alpha_{e(s)} > 0 \end{cases} \tag{36}$$

where C_{N1} defined by:

$$C_{N1} = \frac{dC_N}{d\alpha}(\alpha^{CRIT}_n - \alpha_0) \tag{37}$$

The tangential force component can be calculated by:

$$C^v_{T_{(s)}} = K_{C_T} + C^f_{T_{(s)}} f_{bl}^{\left[D_{C_T}\left(C'_N - C_{N1}\right) + \left(f_{bl} - f_p\right)\right]} \tag{38}$$

The pitching moment term is obtained by:

$$C^v_{M_{(s)}} = -X_{CP.N(s)} C^v_{N_{(s)}} = -0.2\left[1 - cos\left(\frac{\pi\tau_{v(s)}}{T_{vl}}\right)\right] C^v_{N_{(s)}} \tag{39}$$

And finally, the total dynamic normal force coefficients are obtained by:

$$C^{dyn}_{N_{(s)}} = C^v_{N_{(s)}} + C^f_{N_{(s)}} = \frac{dC_N}{d\alpha}\left(\frac{1+\sqrt{f_{bl}}}{2}\right)^2 \left(\alpha_{e(s)} - \alpha_0\right) + C^I_{N_{(s)}} + C^v_{N_{(s)}} \tag{40}$$

$$C^{dyn}_{T_{(s)}} = \begin{cases} C^f_{T_{(s)}} \ ;\ \left|C'_N\right| \le C_{N1} \\ C^v_{T_{(s)}};\ \left|C'_N\right| > C_{N1} \end{cases} \tag{41}$$

$$C^{dyn}_{L_{(s)}} = C^{dyn}_{N_{(s)}} cos\ \alpha + C^{dyn}_{T_{(s)}} sin\alpha \tag{42}$$

$$C^{dyn}_{D_{(s)}} = C_{D0} + \left(C^{dyn}_{N_{(s)}} sin\ \alpha - C^{dyn}_{T_{(s)}} cos\alpha\right) \tag{43}$$

$$C^{dyn}_{M_{(s)}} = C_{M0} + \left[C^C_{M_{(s)}} + \left(C^I_{M,\alpha_{(s)}} + C^I_{M,q_{(s)}}\right)\right] + C^f_{M_{(s)}} + C^v_{M_{(s)}} \tag{44}$$

Appendix 7

See Figs. 13 and 14.

Appendix 8. Nomenclature

Greek symbols
α = angle of attack [°]
α_0 = zero lift angle of attack [°]
α_e = equivalent angle of attack [°]
α_m = mean angle of attack [°]
α^{CRIT}_n = critical angle of attack [°]
α_{qs} = quasi steady angle of attack [°]
ϕ = indicial response function [–]
η = drag recovery factor [–]
τ_v = reduced time [–]

Abbreviations
AOA = angle of attack [°]
$B-L$ = Beddoes-Leishman
BSA = bottom stagnation angle [°]
CFD = computational fluid dynamics [–]
DFR = drag force range, the distance between maximum and minimum C_D [–]
DS = down-stroke [–]
$DSAOA$ = dynamic stall angle of attack [°]
LEV = leading edge vortex [–]
LFR = lift force range, the distance between maximum and minimum C_L [–]
$MLOS$ = maximum lift overshoot [–]
$NMAE$ = normalized mean absolute error [%]
Re = Reynolds number [–]

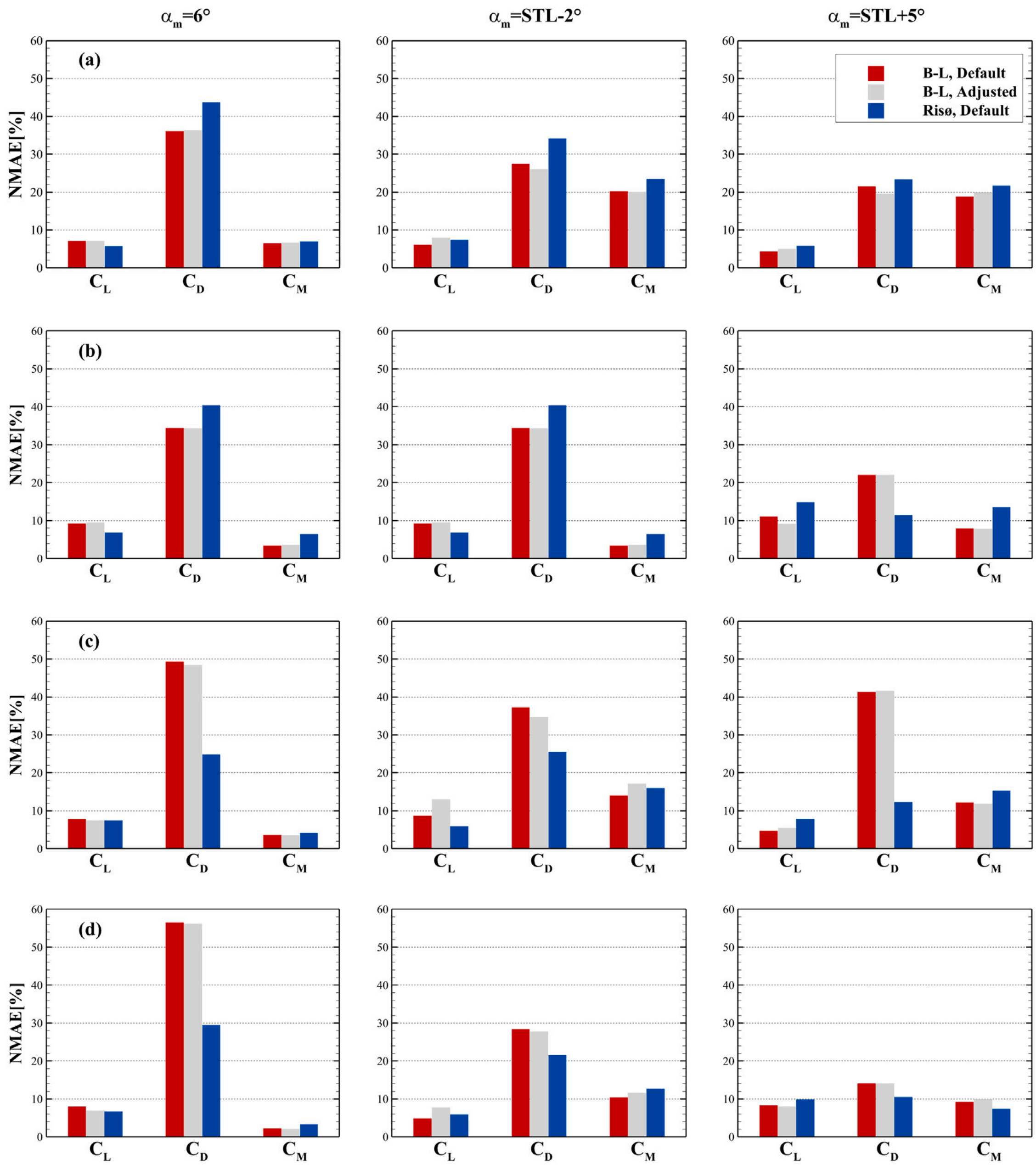

Fig. 13. Variation of the NMAE error for different airfoils at different mean angle of attack [$Re = 1 \times 10^6$, (a) X-35-02, (b) X-35-02, $VGs(x/C) = 0.3$, (c) X-FB-35-10, (d) X-FB-35-10, $k = 0.064$, $VGs(x/C) = 0.3$].

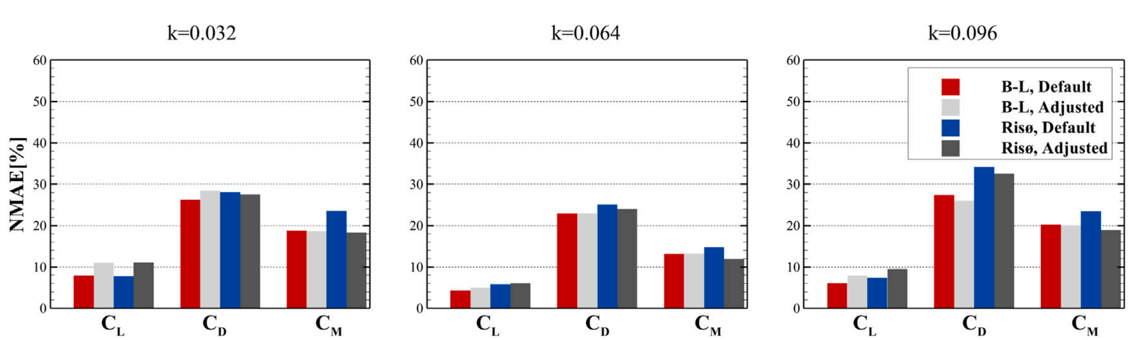

Fig. 14. Variation of the NMAE for different reduced frequencies in free transition flow [$Re = 1 \times 10^6$, X-35-02, $\alpha_m = STL - 2°$].

STL = stall [–]
TSA = top stagnation angle [°]
US = up-stroke [–]
VGs = vortex generators [–]

Symbols

A = amplitude of oscillation [°]
A_i = indicial response function coefficient [–]
b_i = indicial response function coefficient [–]
C = chord [m]
C_D = drag coefficient [–]
C_{D0} = zero lift drag coefficient [–]
C_L = lift coefficient [–]
C_M = moment coefficient [–]
C_M^v = vortex induced moment coefficient [–]
C_{M0} = zero lift moment coefficient [–]
C_N = normal coefficient [–]
C_{N1} = critical normal coefficient [–]
C_N^P = normal force coefficient under potential flow condition [–]
C_N^v = vortex induced normal coefficient [–]
C_T = tangential force coefficient [–]
C_T^v = vortex induced tangential force coefficient [–]
C_v = vortex lift increment [–]
D = deficit function [–]
D_{C_T} = static C_T curve fitting parameter [–]
f = non-dimensional steady separation position [–]
k = reduced frequency [–]
K_{C_T} = static C_T curve fitting parameter [–]
M = Mach number [–]
s = non-dimensional time [–]
t = time [s]
T_p = leading edge pressure peak time constant [–]
T_f = boundary layer separation lag time constant [–]
T_v = leading edge vortex decay constant [–]
T_{vl} = leading edge vortex convection time constant [–]
V = free stream velocity [m/s]
X = deficiency function [–]
X_{CP} = center of the pressure offset [–]
Y = deficiency function [–]

Superscript

C = circulatory quantity [–]
dyn = total dynamic coefficient [–]
f = separated flow quantity [–]
I = non-circulatory quantity [–]
P = total quantity [–]
st = static quantity [–]
$'$ = lagged value [–]

Subscript

bl = unsteady boundary layer lagged value [–]
f = lagged value [–]
max = maximum value [–]

References

[1] THOMAS D. ASHWILL, Parametric Study for Large Wind Turbine Blades: WindPACT Blade System Design Studies, Technical report, Sandia National Lab.(SNL-NM), Albuquerque, NM (United States); Sandia ..., 2002, http://dx.doi.org/10.2172/801402.

[2] Lin Wang, Xiongwei Liu, Athanasios Kolios, State of the art in the aeroelasticity of wind turbine blades: Aeroelastic modelling, Renew. Sustain. Energy Rev. 64 (2016) 195–210, http://dx.doi.org/10.1016/j.rser.2016.06.007.

[3] Gordon J. Leishman, Principles of Helicopter Aerodynamics with CD Extra, Cambridge university press, ISBN 0521858607, 2006.

[4] Ricardo Pereira, Gerard Schepers, Marilena D. Pavel, Validation of the Beddoes–Leishman dynamic stall model for horizontal axis wind turbines using MEXICO data, Wind. Energy 16 (2) (2013) 207–219, http://dx.doi.org/10.1002/we.541.

[5] Max Kramer, Increase in the Maximum Lift of an Airplane Wing Due to a Sudden Increase in Its Effective Angle of Attack Resulting from a Gust, Technical report, 1932.

[6] L.E. Ericsson, Comments on unsteady airfoil stall, J. Aircr. (vol. 4, no. 5) (1967) 478—-480.

[7] Kenneth W. McAlister, Lawrence W. Carr, Water tunnel visualizations of dynamic stall, 1979.

[8] T.S. Beddoes, A qualitative discussion of dynamic stall, in: AGARD Special Course on Unsteady Aerodynamics, AGARD Report, Vol. 679, 1979.

[9] Mrs. M.E. Wood, Results of Oscillatory Pitch and Ramp Tests on the NACA 0012 Blade Section, Aircraft Research Association Limited, 1979.

[10] D. De Tavernier, Carlos Ferreira, A. Viré, B LeBlanc, S Bernardy, Controlling dynamic stall using vortex generators on a wind turbine airfoil, Renew. Energy 172 (2021) 1194–1211, http://dx.doi.org/10.1016/j.renene.2021.03.019.

[11] Amanullah Choudhry, Maziar Arjomandi, Richard Kelso, Methods to control dynamic stall for wind turbine applications, Renew. Energy 86 (2016) 26–37, http://dx.doi.org/10.1016/j.renene.2015.07.097.

[12] J. Gordon Leishman, T.S. Beddoes, A semi-empirical model for dynamic stall, J. Am. Helicopter Soc. 34 (3) (1989) 3–17, http://dx.doi.org/10.4050/JAHS.34.3.3.

[13] Morten Hartvig Hansen, Mac Gaunaa, Helge Aagaard Madsen, A Beddoes-Leishman Type Dynamic Stall Model in State-Space and Indicial Formulations, Denmark. Forskningscenter Risoe. Risoe-R, 2004, Number 1354(EN).

[14] Stig Øye, Dynamic stall simulated as time lag of separation, in: Proceedings of the 4th IEA Symposium on the Aerodynamics of Wind Turbines, Vol. 27, Rome, Italy, 1991, p. 28.

[15] C.T. Tran, D. Petot, Semi-empirical model for the dynamic stall of airfoils in view of the application to the calculation of responses of a helicopter blade in forward flight, 1980.

[16] Franklin D. Harris, Frank J. Tarzanin, Richard K. Fisher, Rotor high speed performance, theory vs. test, J. Am. Helicopter Soc. 15 (3) (1970) 35–44, http://dx.doi.org/10.4050/JAHS.15.35.

[17] Mikhail Goman, Alexander Khrabrov, State-space representation of aerodynamic characteristics of an aircraft at high angles of attack, J. Aircr. 31 (5) (1994) 1109–1115, http://dx.doi.org/10.2514/3.46618.

[18] Hermann Snel, Heuristic modelling of dynamic stall characteristics, in: EWEC-Conference-, Bookshop for Scientific Publications, 1997, pp. 429–433.

[19] Rick R. Damiani, Gregory Hayman, The Unsteady Aerodynamics Module for Fast8, Technical report, National Renewable Energy Lab.(NREL), Golden, CO (United States), NREL/TP-5000-66347, 2019.

[20] Morten Hartvig Hansen, Risø-r-report, 2011.

[21] Matthew Harrison, Menno Kloosterman, Ricard Buils Urbano, Aerodynamic modelling of wind turbine blade loads during extreme deflection events, in: Journal of Physics: Conference Series, Vol. 1037, IOP Publishing, 2018, 062022, http://dx.doi.org/10.1088/1742-6596/1037/6/062022.

[22] P.F. Melani, N. Aryan, L. Greco, A. Bianchini, The Beddoes-Leishman dynamic stall model: Critical aspects in implementation and calibration, Renew. Sustain. Energy Rev. 202 (2024) 114677, http://dx.doi.org/10.1016/j.rser.2024.114677.

[23] Bin Huang, Pengzhong Wang, Lu Wang, Tingfa Cao, Dazhuan Wu, Peng Wu, A combined method of CFD simulation and modified Beddoes-Leishman model to predict the dynamic stall characterizations of S809 airfoil, Renew. Energy 179 (2021) 1636–1649, http://dx.doi.org/10.1016/j.renene.2021.07.131.

[24] Mingwei Ge, Haitao Sun, Hang Meng, Xintao Li, An improved BL model for dynamic stall prediction of rough-surface airfoils, Renew. Energy 226 (2024) 120371, http://dx.doi.org/10.1016/j.renene.2024.120371.

[25] Xiong Liu, Shi Liang, Gangqiang Li, Ajit Godbole, Cheng Lu, An improved dynamic stall model and its effect on wind turbine fatigue load prediction, Renew. Energy 156 (2020) 117–130, http://dx.doi.org/10.1016/j.renene.2020.04.040.

[26] Mark Faber, A Comparison of Dynamic Stall Models and Their Effect on Instabilities Master's Thesis, 2018.

[27] Niels Adema, Menno Kloosterman, Gerard Schepers, Development of a second-order dynamic stall model, Wind. Energy Sci. 5 (2) (2020) 577–590, http://dx.doi.org/10.5194/wes-5-577-2020,2020.

[28] David Greenblatt, Hanns Mueller-Vahl, David R Williams, Florian Reissner, Goman-khrabrov model on a pitching airfoil with flow control, in: 8th AIAA Flow Control Conference, 2016, p. 4240, http://dx.doi.org/10.2514/6.2016-4240.

[29] Kenneth W. McAlister, O. Lambert, D. Petot, Application of the ONERA Model of Dynamic Stall, Technical report, 1984.

[30] Galen Brandt Schubauer, W.G. Spangenberg, Forced mixing in boundary layers, J. Fluid Mech. 8 (1) (1960) 10–32, http://dx.doi.org/10.1017/S0022112060000372.

[31] Daniel Baldacchino, Carlos Ferreira, Delphine De Tavernier, WA Timmer, GJW Van Bussel, Experimental parameter study for passive vortex generators on a 30% thick airfoil, Wind. Energy 21 (9) (2018) 745–765, http://dx.doi.org/10.1002/we.2191.

[32] Hyeongi Moon, Junhee Jeong, Sunho Park, Kwangtae Ha, Jae-Ho Jeong, Numerical and experimental validation of vortex generator effect on power performance improvement in MW-class wind turbine blade, Renew. Energy 212 (2023) 443–454, http://dx.doi.org/10.1016/j.renene.2023.04.104.

[33] Delft university of technology. Low turbulence tunnel (LTT), 2025, https://www.tudelft.nl/lr/organisatie/afdelingen/flow-physics-and-technology/facilities/low-speed-wind-tunnels/low-turbulence-tunnel. (Accessed 16 January 2024).

[34] Biao Lu, Michael Bragg, Experimental investigation of the wake-survey method for a bluff body with a highly turbulent wake, in: 20th AIAA Applied Aerodynamics Conference, 2002, p. 3060, http://dx.doi.org/10.2514/6.2002-3060.

[35] C. Dalton, Allen and vincenti blockage corrections in a wind tunnel, Aiaa J. 9 (9) (1971) 1864–1865, http://dx.doi.org/10.2514/3.6435.

[36] H. Bergh, Hendrik Tijdeman, Theoretical and experimental results for the dynamic response of pressure measuring systems, 1965.

[37] Mehdi Doosttalab, Carlos Simao Ferreira, Daniele Ragni, Wei Yu, Christof Rautmann, Vortex generator effects on dynamic stall of thick airfoils, Renew. Energy (2025) 123746, http://dx.doi.org/10.1016/j.renene.2025.123746.

[38] Sandeep Gupta, J. Gordon Leishman, Dynamic stall modelling of the S809 aerofoil and comparison with experiments, Wind. Energy: An Int. J. Prog. Appl. Wind. Power Convers. Technol. 9 (6) (2006) 521–547, http://dx.doi.org/10.1002/we.200.

[39] J. Gordon Leishman, Indicial lift approximations for two-dimensional subsonic flow as obtained from oscillatory measurements, J. Aircr. 30 (3) (1993) 340–351, http://dx.doi.org/10.2514/3.46340.

[40] T.S. Beddoes, Practical computation of unsteady lift, 1982.

[41] J. Gordon Leishman, Assessment of Aerodyn Theory Basis Including Unsteady Aerodynamics Modules, Technical report, Technical report, Rotor Systems Research LLC, 2011.

[42] T.J. Larsen, A.M. Hansen, How 2 HAWC2, The User's Manual (Ver 12.9), Technical report, Tech. Rep. Risø, 2021.

[43] J.G. Leishman, T.S. Beddoes, A generalized method for unsteady airfoil behaviour and dynamic stall using the indicial method 42nd Annual Forum of the AHS, 1986.

[44] J.G. Leishman, T.S. Beddoes, A generalised model for airfoil unsteady aerodynamic behaviour and dynamic stall using the indicial method, in: Proceedings of the 42nd Annual Forum of the American Helicopter Society, Vol. 34, Washington DC, 1986, pp. 3–17.

[45] Octavian Frederich, Ulf Bunge, Charles Mockett, Frank Thiele, Flow prediction around an oscillating naca0012 airfoil at re = 1,000,000, in: IUTAM Symposium on Unsteady Separated Flows and their Control: Proceedings of the IUTAM Symposium "Unsteady Separated Flows and their Control ", Corfu, Greece, 18–22 June 2007, Springer, 2009, pp. 49–62, http://dx.doi.org/10.1007/978-1-4020-9898-7_5.

[46] Dale Berg, Jose Zayas, Aerodynamic and aeroacoustic properties of flatback airfoils, in: 46th AIAA Aerospace Sciences Meeting and Exhibit, 2008, p. 1455, http://dx.doi.org/10.2514/6.2008-1455.

[47] Chris C. Critzos, Harry H. Heyson, Robert W. Boswinkle Jr., Aerodynamic Characteristics of NACA 0012 Airfoil Section at Angles of Attack from 0 Degrees to 180 Degrees, Technical report, NASA, NACA-TN-3361, 1955.

[48] T.S. Beddoes, Onset of leading edge separation effects under dynamic conditions and low mach number, in: American Helicopter Society, Annual National Forum, 34 Th, Washington, D. C, Proceedings, Research Supported By the Ministry of Defence,(Procurement Executive), Vol. 15, 1978.

[49] J. Gordon Leishman, Validation of approximate indicial aerodynamic functions for two-dimensional subsonic flow, J. Aircr. 25 (10) (1988) 914–922, http://dx.doi.org/10.2514/3.45680.